

Trace element composition of scheelite in orogenic gold deposits — Source link

Marjorie Sciuba, Georges Beaudoin, Donald Grzela, Sheida Makvandi

Institutions: Laval University

Published on: 01 Aug 2020 - Mineralium Deposita (Springer Berlin Heidelberg)

Topics: Scheelite, Metamorphic facies, Greenschist and Felsic

Related papers:

- [Rare earth element systematics in scheelite from hydrothermal gold deposits in the Kalgoorlie-Norseman region, Western Australia](#)
- [Trace elements and Sr-Nd isotopes of scheelite: Implications for the W-Cu-Mo polymetallic mineralization of the Shimensi deposit, South China](#)
- [Scheelite elemental and isotopic signatures: Implications for the genesis of skarn-type W-Mo deposits in the Chizhou Area, Anhui Province, Eastern China](#)
- [Inhomogeneous distribution of REE in scheelite and dynamics of Archaean hydrothermal systems \(Mt. Charlotte and Drysdale gold deposits, Western Australia\)](#)
- [Trace element geochemistry of scheelite and rutile from metaturbidite-hosted quartz vein gold deposits, Meguma Terrane, Nova Scotia, Canada: genetic implications](#)

Share this paper:    

View more about this paper here: <https://typeset.io/papers/trace-element-composition-of-scheelite-in-orogenic-gold-17uxzorl2i>

Trace element composition of scheelite

Marjorie Sciuba^{1,2}, Georges Beaudoin^{1,2}, Donald Grzela^{1,2}, Sheida Makvandi^{1,2,3}

✉ Marjorie Sciuba

Marjorie.Sciuba.1@ulaval.ca

✉ Georges Beaudoin

Georges.Beaudoin@ggl.ulaval.ca

1 Département de Géologie et Génie Géologique, Université Laval, Québec (QC) G1V 0A6, Canada

2 Centre de recherche sur la géologie et l'ingénierie des ressources minérales (E4m)

3 COREM, 1180 Rue de la Minéralogie, Québec, Canada, G1N 1X7

10

11

12 **Abstract** Scheelite from twenty-five representative orogenic gold deposits from various geological settings was
13 investigated by EPMA (Electron Probe Micro-Analyzer) and LA-ICP-MS (Laser Ablation-Inductively Coupled Plasma-Mass
14 Spectrometer) to establish discriminant geochemical features to constrain indicator mineral surveys for gold exploration.
15 Scheelite from orogenic gold deposits displays five REE patterns including a bell-shaped pattern with a (i) positive or (ii)
16 negative Eu anomaly; iii) a flat pattern with a positive Eu anomaly and, less commonly, iv) a LREE enriched pattern, and v)
17 a HREE enriched pattern. The REE patterns are interpreted to reflect the source of the auriferous hydrothermal fluids and,
18 perhaps, co-precipitating mineral phases. Scheelite from deposits formed in rocks metamorphosed at upper greenschist to
19 lower amphibolite facies have low contents in REE, Y, and Sr, and high contents in Mn, Nb, Ta and V, compared to scheelite
20 formed in rocks metamorphosed below the middle greenschist facies. Scheelite from deposits hosted in sedimentary rocks has
21 high Sr, Pb, U and Th, and low Na, REE and Y, compared to that hosted in felsic to intermediate rocks. Statistical analysis
22 including elemental plots and multivariate statistics with PLS-DA (Partial Least Square-Discriminant Analysis) reveal that
23 the metamorphic facies of the host rocks, as well, as the regional host rock composition exert a strong control on scheelite
24 composition. This is a result of fluid-rock exchange during fluid flow to gold deposition site. PLS-DA and elemental ratio
25 plots show that scheelite from orogenic gold deposits have distinct Sr, Mo, Eu, As and Sr/Mo, but indistinguishable REE
26 signatures, compared to scheelite from other deposit types.

27 **Keywords** scheelite, orogenic gold deposits, trace elements, cathodoluminescence, principal component analysis,
28 partial least square-discriminant analysis

29

Introduction

30 The association between gold and scheelite in orogenic gold deposits has long been recognized. Goldfarb et al. (2005)
31 review the characteristics of orogenic gold deposits. In many deposits, scheelite predates and/or is contemporaneous with gold
32 deposition, such as in the Val-d'Or district, Canada (Beaudoin and Pitre 2005), at Mt. Charlotte, Australia (Mueller 1991) or
33 Charmitan, Uzbekistan (Graupner et al. 2010). Scheelite is a major mineral in greisen and skarn (Xiong et al. 2006; Ren et al.
34 2010; Song et al. 2014; Guo et al. 2016; Poulin 2016; Poulin et al. 2016; Poulin et al. 2018), and a minor mineral in Cu-(Mo-
35 Au) porphyry deposits (Poulin 2016; Poulin et al. 2016; Sun and Chen 2017; Poulin et al. 2018), where it occurs in veins or
36 disseminated in altered rocks. Scheelite is also an accessory mineral in aplite, pegmatite and metamorphosed sedimentary
37 exhalative Fe-Mn (Brugger et al. 1998; Uspensky et al. 1998) and volcanogenic massive sulphides deposits (Poulin 2016;
38 Poulin et al. 2016; Poulin et al. 2018).

39 The indicator mineral technique is used in exploration using overburden sediments for several deposit types.
40 Discriminant geochemical features in major, minor and trace elements of indicator minerals may be used to recognize a
41 deposit type. For instance, Cr-rich spinel and Cr-rich garnet are indicators for diamond-bearing kimberlite (Gurney 1984;
42 Fipke et al. 1995; McClenaghan and Kjarsgaard 2007), and Ni-Cu mineralization (Aumo and Salonen 1986; Peltonen et al.
43 1992; Somarin 2004), whereas magnetite has been shown to be useful to fingerprint various mineral deposit types (Dupuis
44 and Beaudoin 2011; Boutroy et al. 2014; Dare et al. 2014). Scheelite is considered an indicator mineral for orogenic gold
45 (McClenaghan and Cabri 2011) and tungsten deposits (Lindmark 1977; Toverud 1984; Johansson et al. 1986). In indicator
46 mineral surveys, scheelite is recovered from the heavy mineral fraction or overburden sediments, but the deposit type at the
47 source of the scheelite grains cannot, currently, be determined.

48 Scheelite (CaWO_4) and powellite (CaMoO_4) form a partial solid solution where Mo^{6+} substitutes for W^{6+} (Tyson et
49 al. 1988). Pure scheelite is bluish under short wave fluorescent light, whereas Mo-rich scheelite is typically yellow in color
50 (Van Horn 1930; Shoji and Sasaki 1978). Scheelite is luminescent under an electron beam allowing to study textural zonation
51 and successive scheelite generations in relationship with their trace element composition. The REE, Y, As, and Sr content in
52 scheelite have a minor effect on the cathodoluminescence (CL) response (Brugger et al. 2000a; MacRae et al. 2009; Poulin
53 2016; Poulin et al. 2016), whereas Mo variation is associated with CL zoning, (Poulin 2016; Poulin et al. 2016). The CL
54 zoning may result from primary crystallization or from multi-stage evolution (Brugger et al. 2000a).

55 Replacement of W by Mo and Ca by Sr, Pb, Fe, Mn, Ba and REE have been reported (Cottrant 1981; Rimbault et
56 al. 1993; Ghaderi et al. 1999) and traces of Na, V, Nb, Ta, S, As, Pb, U, Th, Mn, Fe, Au, Ba, B, Co, Cr, K, Ni, Sb, Sc, Zn, Bi,

57 Cu, Sn, Zn, Li, Ti and Rb have been measured in variable amounts in scheelite from various types of deposits (Anglin 1992;
58 Eichhorn et al. 1997; Zhigang et al. 1998; Ghaderi et al. 1999; Brugger et al. 2000a; Brugger et al. 2000b; Brugger et al. 2002;
59 Xiong et al. 2006; Liu Yan et al. 2007; Dostal et al. 2009; Graupner et al. 2010; Peng et al. 2010; Ren et al. 2010; Song et al.
60 2014; Hazarika et al. 2016; Poulin 2016; Poulin et al. 2016; Fu et al. 2017; Sun and Chen 2017). The high REE concentrations
61 (~10-5,000 ppm; Uspensky et al. 1998) in scheelite have been used for Sm-Nd geochronology in order to date the gold
62 mineralization (Anglin 1992; Anglin et al. 1996; Frei et al. 1998; Uspensky et al. 1998; Kempe et al. 2001; Roberts et al.
63 2006) whereas the Sr and Nd isotopic compositions have been used to constrain the sources and the pathway of auriferous
64 hydrothermal fluids (Bell et al. 1989; Mueller et al. 1991a; Kent et al. 1995; Darbyshire et al. 1996; Frei et al. 1998). Most of
65 the studies on Sr and Nd isotopic composition of scheelite from orogenic gold deposits conclude that the fluids are derived
66 from the mantle and/or the lower crust (Bell et al. 1989; Mueller et al. 1991a; Darbyshire et al. 1996; Voicu et al. 2000), with
67 the exception of the Muruntau gold deposit where Kempe et al. (2001) concluded that fluids were most probably derived from
68 the local host rocks. Calcium is likely derived from the regional host rocks, whereas, W is considered to be derived from the
69 hydrothermal fluids (Goldfarb and Groves 2015). Isotopic studies of scheelite have shown that Sr is partly derived from the
70 local host rocks (Mueller et al. 1991a; Darbyshire et al. 1996; Ghaderi et al. 1999; Brugger et al. 2002), whereas Pb and Nd
71 have more complex sources at the local and regional scales (Brugger et al. 2002). Poulin (2016) discriminated the trace
72 element signatures of metamorphic scheelite to that from magmatic and hydrothermal settings using the Eu anomaly vs Mo/Sr.
73 Previous studies, however, do not provide a common, comprehensive, set of minor and trace elements contents in orogenic
74 gold deposit scheelite.

75 Defining the texture, luminescence properties, and trace element composition of scheelite from orogenic gold
76 deposits could be used to identify and track these deposits in overburden sediments. In this study, we present textural and
77 chemical characteristics of scheelite from 25 orogenic gold deposits, including 13 world-class examples, that represent a large
78 variation in host rock composition and age, metamorphic facies and mineralization age, in order to characterize scheelite from
79 this deposit type. Mineral texture was investigated by CL and composition was determined by Electron Probe Micro Analyzer
80 (EPMA) for major and minor elements, and by Laser Ablation-Inductively Coupled Plasma-Mass Spectrometry (LA-ICP-
81 MS) for minor and trace elements. Discriminant binary and ternary diagrams, box plots and multivariate statistics including
82 Principal Component Analysis (PCA) and Partial Least Square-Discriminant Analysis (PLS-DA) are used to characterize
83 scheelite composition from various geological settings within the orogenic gold deposit type. Furthermore, we compare the
84 chemical composition of scheelite from orogenic gold deposits to that from other deposit types in order to define discriminant
85 criteria that would be useful to identify the source of scheelite in indicator mineral surveys.

86 **Geological settings of the selected orogenic gold deposits**

87 Typical samples of gold mineralization were selected from 13 world-class (Goldfarb et al. 2005) and 12 additional
88 orogenic gold deposits and districts (ESM 1a). The set of samples is considered to represent largely the variability of orogenic
89 gold deposit characteristics. The origin of the Kumtor, Canadian Malartic and Young Davidson deposits is still debated, but
90 we follow Goldfarb et al. (2005) and consider they belong to the orogenic type. Mueller (1997) and Mueller et al. (2004)
91 considered the Nevoria gold deposit as a skarn, whereas Eilu et al. (1999) and Goldfarb et al. (2005) classified it as an orogenic
92 gold deposit. In the following, Nevoria is described with the other orogenic gold deposits. In addition, we report on the
93 Crusader deposit that has been interpreted to be intrusion-related (Jowitt et al. 2014). Deposits were selected to provide a
94 representative range of geological settings (ESM 1a). Host rocks consist of sedimentary (clastic, black shale, banded-iron
95 formation), volcanic (basalt, komatiite) and plutonic rocks (syenite, granite, granodiorite, tonalite, diorite, gabbro). The
96 selected gold deposit host rocks are metamorphosed from the lower greenschist (e.g., Paddington, Sigma-Lamaque) to the
97 mid-amphibolite facies (e.g., Marvel Loch, Edward's Find). To simplify comparison, deposits hosted in lower greenschist
98 facies rocks and below are labelled low metamorphic, deposits in mid-greenschist facies rocks are considered moderate
99 metamorphic and deposits in upper greenschist to lower amphibolite facies rocks are labelled high metamorphic. Scheelite
100 has not been described in orogenic gold deposits hosted in higher grade metamorphic rocks such as Challenger, Griffin's Find,
101 or Renco. Most of the deposits selected formed during the Archean (e.g., Hutti) but our selection includes deposits formed
102 during the Proterozoic (e.g., Essakane), the Paleozoic (e.g., Kumtor) and the Mesozoic (e.g., Macraes). Host rock ages range
103 from Archean to Paleozoic (ESM 1a). In the selected deposits, scheelite occurs in the mineral assemblage of the gold
104 mineralization.

105 **Scheelite texture and mineral assemblages**

106 Scheelite is commonly pinkish to whitish beige at the macroscopic scale. Scheelite occurs most commonly as
107 centimeter-size aggregates of massive anhedral grains free of inclusions such as at Beaufor, Sigma, Dome, Canadian Malartic,
108 Cuiaba (Fig. 1a), Essakane, Macraes, and Crusader. Scheelite locally forms isolated subhedral grains at Canadian Malartic
109 (Fig. 1b) and Paddington. Scheelite is finely disseminated (50-500 μm) at Rosebel, Kochkar (Fig. 1d), Kumtor, Navachab,
110 Buzwagi and Transvaal. Grain aggregates locally form veinlets at Kumtor (Fig. 1e). At Hutti, scheelite shows a polygonal
111 fabric typical of dynamic recrystallization (Fig. 1c).

112 Mineral associations are detailed for each deposit in ESM 1b. Scheelite is most commonly associated with quartz,
113 carbonates, amphiboles, tourmaline, sericite, muscovite, feldspar, clinopyroxene, magnetite, pyrite and arsenopyrite.
114 Accessory minerals associated with scheelite are rutile, titanite, hematite, chalcopyrite and pyrrhotite. Native gold forms
115 inclusions in pyrite which is in textural equilibrium with scheelite at Paddington and Tarmoola (Fig. 1h). At Crusader, native
116 gold is in textural equilibrium with scheelite, in association with magnetite and muscovite (Fig. 1i). At Rosebel and Hutti,
117 scheelite occurs in the same sample as native gold but is not in textural equilibrium. At Norseman, coarse-grained scheelite
118 aggregates are intergrown with minor sphalerite, galena and rare native gold (Mueller 1990). All scheelite grains display
119 homogeneous blue fluorescence under UVC light, with the exception of samples from the Crusader and Nevorio deposits,
120 which exhibit a yellow colour.

121 **Analytical methods**

122 **Sample preparation**

123 Scheelite-bearing samples were collected from the selected deposits, or donated by researchers or mining companies
124 (ESM 1a). Thirty-seven polished thin sections from 25 deposits were studied using the petrographic microscope. An additional
125 five samples, from the Hollinger, Dome, Young Davidson, Sigma and Cuiaba deposits were disaggregated by Electrical Pulse
126 Disaggregation (EPD) at Overburden Drilling Management (Ottawa) to recover ultra-trace scheelite. Scheelite grains were
127 hand-picked under the binocular microscope and UVC light from the non-magnetic, heavy (SG > 3.3), 0.25-0.5 mm and 0.5-
128 1.0 mm grain size fractions. Scheelite was recovered from the EPD samples from Hollinger, Young Davidson and Sigma,
129 whereas, samples from the Dome and Cuiaba deposits contained no scheelite. Scheelite grains recovered by EPD were
130 mounted in epoxy polished sections. Scheelite grains from Marvel Loch (Mueller 1991; Mueller et al. 1991b), Nevorio
131 (Mueller 1997; Mueller et al. 2004), Edward's Find (Schwebel et al. 1995), Mount Pleasant (Cassidy and Bennett 1993), Mt.
132 Charlotte (Mueller 2015), Paddington (Hancock et al. 1990) and Norseman (Australia; Mueller 1992) were donated by A.
133 Mueller (ESM 1a) and mounted in epoxy polished section.

134 **Electron Probe Micro-Analysis (EPMA)**

135 We analysed 145 spots from 25 deposits by EPMA (ESM 2b). The major and minor element composition of scheelite was
136 measured at Université Laval using a CAMECA SX-100, equipped with five wavelength-dispersive spectrometers (WDS).
137 Major elements W and Ca were measured with a beam current of 20 nA with an accelerating voltage at 15 kV, for 20 s for

138 the peak and 10 s for the background, using a beam diameter of 10 μm . Metal tungsten (W-ATX) and diopside were used as
139 standards for W and Ca. Concentrations of Na, Sr, Mo, Y and Fe were measured with a 10 μm diameter beam with a current
140 of 100 nA, an accelerating voltage of 15 kV, and counting times of 120 s for the peak and 30 s for the background. Metal
141 molybdenum (Mo-ATX) for Mo, celestite for Sr, YPO_4 for Y, hematite for Fe and albite for Na were used as standards (ESM
142 2a). Carbonates were measured for major and minor elements including Ca, Fe, Mg, Mn and Sr using a beam diameter of 10
143 μm , a current of 20 nA and an accelerating voltage at 15 kV. Cathodoluminescence imaging was performed at 15 kV and 20
144 nA with a CAMECA cathodoluminoscope. The CL was recorded as grey-scale images to document textures and zonation in
145 scheelite.

146 **Laser Ablation-Inductively Coupled Plasma-Mass Spectrometry (LA-ICP-MS)**

147 We conducted 146 analyses, including 125 lines and 35 spots, and 7 maps from 24 deposits (ESM 2d) by LA-ICP-MS at
148 LabMaTer, Université du Québec à Chicoutimi (UQAC) using a RESolution M-50 Excimer 193 nm laser coupled to an
149 Agilent 7700x ICP-MS with a frequency of 10 Hz and a power of 5.4 $\text{mJ}\cdot\text{cm}^{-2}$. The beam size was set at 44 μm for lines and
150 spots and 33 μm for maps. Line analyses are preferred to spots for large grains. The background was counted for 30 s and the
151 acquisition time was 60 s. Scan speed was fixed at 20 mm/s for the large grains, spots and maps and 10 mm/s for grains less
152 than ca. 300 μm wide. The reference material NIST-610, NIST-612, GSD-1g-A, GSE-1g-A (Jochum et al. 2005) and
153 Gprobe6-A were used for calibration. NIST-610, GSD-1g-A and Gprobe6-A were analysed before and after a run. NIST-612
154 and GSD-1g-A were measured every hour during analytical sessions. Details for external standards are provided in ESM 2c.
155 Calcium⁴⁴ was used as the internal standard and fixed at 13.90 wt. %, based on the average EPMA composition. Data were
156 reduced using the Iolite software. Detection limits (DL) are summarized in ESM 2c.

157 Electron Probe Micro-Analysis and LA-ICP-MS analyses give the chemical composition at two different scales and
158 are therefore complementary (10 μm beam size for EPMA versus about 1000x40 μm for LA-ICP-MS line analysis). Ablation
159 lines allow to document zonation and are more representative of the bulk composition of the grain, whereas EPMA analyses
160 provide spatially resolved chemical composition. Comparison between EPMA and LA-ICP-MS data (ESM 3a) shows a good
161 correlation between the two instruments, except close to the detection limit. Scheelite does not contain inclusions at the
162 microscope scale, however, peaks in Fe-Mg-Si correlated with a sharp decrease in W and Ca in the LA-ICP-MS spectra, and
163 shows that scheelite contain locally Fe-Mg-Si-rich sub-microscopic inclusions that were excluded in data reduction.

164 **Statistical analysis**

165 Data were investigated using both basic and multivariate statistics such as Principal Component Analysis (PCA) and
166 Partial Least Square-Discriminant Analysis (PLS-DA). Electron probe microanalysis and LA-ICP-MS datasets are typically
167 censored because they contain non-detects that are below the detection limit (Helsel 2005). Censored compositional data were
168 imputed using the k-nearest neighbor function with the Aitchison distance (robCompositions package in R; Hron et al. 2010;
169 Makvandi et al. 2016b). Geochemical data, summed to 100%, can lead to spurious correlations, inherent to all compositional
170 datasets (Aitchison 1986; Whitten 1995). Data were transformed using centered-log ratio (clr; Thió-Henestrosa and Martín-
171 Fernández 2005) that is a suitable method for multivariate statistical analysis (Aitchison 1986; Egozcue et al. 2003; Makvandi
172 et al. 2016b)

173 Silica, Cr, Sn and Ag were excluded from the PCA and PLS-DA because more than 40 % of the data are below
174 detection limit (DL). Both methods plot highly positively correlated variables together in same quarter in the principal
175 components diagram, whereas, inversely correlated variables plot in opposite quarters. PCA is a non-supervised statistical
176 method that captures the maximum variance among the data set, whereas PLS-DA is a supervised statistical method of
177 classification that uses labeled data (de Iorio et al. 2007). In PLS-DA, a series of orthogonal components relate to the X ($N \times$
178 K) and Y ($N \times M$) matrices by maximizing the covariance between the two. Loadings biplots (q_{w*1} - q_{w*2}) indicate the
179 correlation among different elements, and the relationship between the variables and different sample classes (e.g., host rock
180 composition). The loading values show the impact of elements on the model, and the sign of the value indicates the positive
181 or negative correlation between the elements. As a result, elements that plot in the vicinity of each other in the PLS-DA
182 loadings space show strong positive correlation, and they are inversely correlated to those in an opposite quadrant. The
183 correlation among variables and sample classes control the distribution of samples in the score scatter plot (t_1 - t_2). The origin
184 of score scatter plots represents the mean composition of the whole dataset (Makvandi et al. 2016b). The Variable Importance
185 on Projection (VIP) plots are used to indicate the impact of different variables on the sample classification, where VIP values
186 equal and/or larger than 1 are the most important in the classification (Eriksson et al. 2001).

187 **Results**

188 **Cathodoluminescence and trace elements variation**

189 Scheelite from orogenic gold deposits commonly exhibits homogeneous cathodoluminescence (Fig. 2a), with brighter local
190 patches in rare samples, whereas, sub-grains can be distinguished within a larger grain (Fig. 2b). Scheelite from the Macraes

191 deposit consists of at least two generations: (1) a first generation that forms most of the grain, (2) younger veinlets with darker
192 CL that cut the first scheelite (Fig. 3b). The two generations of scheelite from the Macraes deposit differ in the trace element
193 composition (Fig. 3). The early, bright CL scheelite, has high Sr, Na, Mg, Mn, Th and U, and low REE and Y contents (Fig.
194 3b). The second generation of vein and breccia scheelite is darker in CL and associated with low Sr, Na, Mg, Mn, Th, and U
195 and high REE and Y contents (Fig. 3b). Dark CL breccia cuts the edge of scheelite grains from Macraes, Crusader (Fig. 2f)
196 and Mount Pleasant (Fig. 2e). Scheelite veinlets cut older scheelite at the Tarmoola deposit (Fig. 2d). Growth zoning in
197 scheelite at Kochkar (Fig. 2g) and Kumtor, where oscillatory zoning is associated with large variations in Sr, Pb, Y, Th and
198 U contents and small variations in As, Na and V. However, the small grain size (ca. 450 μm) and the narrow zones (20 to 150
199 μm) compared to the laser beam diameter (44 μm) complicate the trace element quantification of each zone. Scheelite from
200 the Crusader and Essakane deposits show both sector and oscillatory zoning under CL (Fig. 2i). The oscillatory zoning in
201 Crusader shows a dark zone with high contents in Na, V, As, Nb, REE and Y, and a low Mo, whereas, bright zones have low
202 Na, V, As, Nb, REE and Y and high Mo contents (ESM 3d). Laser ablation-ICP-MS maps of grains with homogeneous CL
203 show little-to-no variation in trace element compositions (Fig. 4).

204 **Trace element composition**

205 Strontium, Si, S and Y have median concentrations over 100 ppm, whereas, Na, Ce, Nd, Dy, Fe, Eu, Gd, Pb, Er, Sm
206 and Yb have median concentration over 10 ppm (ESM 3b). Lanthanum, K, As, Mg, Pr, Ho, Mn, Tb, Cr, Mo, Tm, Nb, Lu and
207 B have median concentration between 1 and 10 ppm. Zinc, Ba, Li, Cu, Ti, V, Sn, U, Th, Ta, Ag and Co have median
208 concentrations between 1 and 0.01 ppm. More than 40% of Si, Cr, Sn, Cr and Ag analyses are below detection.

209 **Rare earth elements and yttrium**

210 Rare Earth Element (REE) patterns for each deposit are shown in ESM 3e and f. Rare earth elements display five
211 patterns with a scheelite/chondrite ratio from 0.2 to 4000, but most are near 100 (Fig. 5): 1) a bell-shaped pattern with a
212 positive (Fig. 5a) or 2) a negative Eu anomaly (Fig. 5c); 3) a flat pattern with a positive Eu anomaly (Fig. 5b); 4) a LREE
213 enriched pattern with small positive to no Eu anomaly (Fig. 5d) and 5) a HREE enriched pattern with positive to no Eu
214 anomaly (Fig. 5e). Rare earth elements normalized to the North American Shale Composite (NASC; Fig. 5; Gromet et al.
215 1984) show a ratio varying from 1 to 100 order of magnitude. Few analyses show a weak depletion in Middle REE (MREE)
216 that are marginally distinct from the flat pattern and, are here included with the flat pattern group in this description (ESM
217 3e). Most scheelite grains show a single REE pattern (ESM 3e and f). The bell-shaped and flat patterns represents, 33 % and
218 40 % of the analyses, respectively. Scheelite from Paddington, Tarmoola, Norseman, Mt. Charlotte and Macraes, displays

219 both bell-shaped and flat patterns with positive Eu anomalies (ESM 3e and f). In the Macraes deposit, early scheelite has a
220 flat pattern, whereas, the later breccia scheelite shows a bell-shaped pattern, both with a positive Eu anomaly (Fig. 3c).
221 Scheelite from deposits hosted in low metamorphic facies rocks commonly present positive Eu anomalies (Essakane,
222 Paddington, Macraes; ESM 3e and f). Several deposits hosted in moderate to high metamorphic grade rocks show strong
223 variations of Eu anomalies, such as Tarmoola, Norseman, Mt. Charlotte (ESM 3f).

224 The LREE-enriched pattern is found in scheelite from the Young Davidson, Kochkar and Kumtor deposits (Fig. 5;
225 ESM 3e). Kochkar scheelite is associated with calcite and has a lower REE content than scheelite in samples free of carbonates
226 (ESM 3c and e). However, both have similar LREE-enriched pattern (ESM 3e). Scheelite from Young Davidson and Canadian
227 Malartic have a LREE-enriched pattern in addition to the more common bell-shaped pattern (ESM 3e). The LREE-enriched
228 pattern has a shape similar to that of NASC (Fig. 5d). Scheelite from the Crusader deposit and the Type-II scheelite at Hutti
229 (Hazarika et al. 2016) have HREE-enriched patterns (Fig. 5e; ESM 3e). The REE pattern of scheelite from the Crusader
230 deposit is similar in both CL zones (ESM 3d). Scheelite from Nevoria exhibits a REE pattern different from that of other
231 orogenic gold deposits, with a flat REE pattern and a scheelite/chondrite ratio of about 10 and no Eu anomaly (Fig. 5f).

232 Binary plots of $(La/Sm)_{CN}$ vs. $(Gd/Yb)_{CN}$ allows easy comparison of LREE- and HREE-enrichment patterns (Fig.
233 6a). Scheelite from orogenic gold deposits plots along a line with a negative slope in that diagram. Scheelite with bell-shaped
234 REE patterns and negative Eu anomaly have low $(La/Sm)_{CN}$ (median 0.03) and high $(Gd/Yb)_{CN}$ (median 10) . Scheelite with
235 bell-shaped REE patterns with a positive Eu anomaly have intermediate $(La/Sm)_{CN}$ (median 0.2) and high $(Gd/Yb)_{CN}$ (~ 5) .
236 Scheelite with a flat REE pattern has $(La/Sm)_{CN}$ and $(Gd/Yb)_{CN}$ ratios near 1 (median 0.9 and 1, respectively). Scheelite with
237 HREE-enriched patterns has low $(La/Sm)_{CN}$ (median 0.12) and $(Gd/Yb)_{CN}$ (median 1.6) , whereas, scheelite with LREE-
238 enriched patterns has high $(La/Sm)_{CN}$ (median 1) and $(Gd/Yb)_{CN}$ (median 10; Fig. 6a). REE patterns with a negative Eu
239 anomaly are characterized by high Na content (median 156 ppm; Fig. 7b).

240 Yttrium concentration ranges from 2.14 to 1680 ppm. Yttrium displays a correlation with the REE (Fig. 7h). Scheelite
241 from deposits formed during the Archean, Proterozoic and Phanerozoic have comparable $\sum REE$ and Y contents (Fig. 7h).
242 Scheelite from deposits hosted in felsic to intermediate rocks have high $\sum REE$ (median 645 ppm and 1164 ppm, respectively)
243 and Y contents (median 348 ppm and 605 ppm, respectively), whereas, scheelite from deposits hosted in sedimentary rocks
244 have lower $\sum REE$ (median 195 ppm) and Y contents (median 113 ppm). Scheelite from deposits hosted in mafic to ultramafic
245 rocks overlap the scheelite composition from deposits hosted in felsic to intermediate rocks, and in sedimentary rocks ($\sum REE$:
246 5-3900 ppm and Y: 5-1700 ppm; Fig. 7h). The Eu anomaly is typically negative or close to zero for scheelite hosted in felsic
247 to intermediate composition rocks (Fig. 7b). Scheelite from deposits in low and moderate metamorphic grade rocks have

248 higher Σ REE (median 334 ppm and 632 ppm, respectively) and Y (median 145 ppm and 253 ppm, respectively) contents
249 compared to scheelite from deposits in high metamorphic grade rocks (median Σ REE 101 ppm and Y 37 ppm; Fig. 7h).

250 **Strontium and lead**

251 Strontium in scheelite from orogenic gold deposits ranges from 83 to 7300 ppm, with a mean of 1244 ppm and a
252 median of 653 ppm (Fig. 8a). The EPMA concentrations for Sr are commonly lower than the LA-ICP-MS values when
253 approaching the EPMA detection limit (ESM 3a). Scheelite from Phanerozoic sedimentary host rocks has higher Sr
254 concentrations (median 3160 ppm) than those from Proterozoic and Archean host rocks (median 2478 ppm and 576 ppm
255 respectively; Fig. 7d and e). Scheelite from deposits hosted in sedimentary and felsic rocks has high Sr contents (median 2890
256 ppm and 811 ppm, respectively) compared to deposits hosted in mafic and ultramafic rocks (median 548 ppm). Scheelite
257 hosted in low and moderate metamorphic grade rocks have Sr contents (median 661 ppm and 1278 ppm, respectively), higher
258 than those hosted in higher metamorphic grade rocks (median 442 ppm; Fig. 7d). Scheelite from Crusader has low Sr
259 concentrations compared to scheelite from the other deposits studied (median 121 ppm). Strontium and Pb data show a positive
260 correlation (Fig. 7f), such that scheelite Pb composition similarly varies with the metamorphic grade of the host rocks, except
261 for Macraes deposit which has low Pb concentrations (median 6 ppm) compared to other low metamorphic grade sedimentary
262 rock hosted deposits (median 28 ppm). The binary diagram Σ REE+Y vs. Sr (Fig. 7d) allows the discrimination of scheelite
263 from low and moderate metamorphic facies host rocks, which typically have higher Σ REE+Y and Sr contents, than scheelite
264 hosted in high metamorphic grade rocks.

265 **Molybdenum**

266 Molybdenum concentrations in scheelite from orogenic gold deposits does not vary significantly in terms of host
267 rock composition, metamorphic grade and age of mineralization. High Mo scheelite from Crusader and Nevoria display a
268 yellow colour under UVC light (median 6.3 wt % and 1.3 wt % Mo, respectively; Fig. 8b). Scheelite from the Canadian
269 Malartic, Kochkar and Kumtor deposits has a relatively high Mo content and are more whitish under UVC light, (median
270 1395 ppm; 383 ppm and 203 ppm, respectively, ESM 2b and d).

271 **Sodium**

272 Sodium concentrations by EPMA and LA-ICP-MS covary moderately ($R^2=0.37$; ESM 3a). EPMA data for Na are
273 commonly higher than LA-ICP-MS data (Fig. 8) perhaps due to sample heterogeneity at the scale of the laser beam spot, as
274 reference material monitoring is good and Na varies in zoned scheelite. Sodium concentration by LA-ICP-MS is highly
275 variable in scheelite from Kochkar ($\bar{X}=133 \pm 256$ ppm; n=19) and in scheelite from Beaufor ($\bar{X}=183 \pm 94$ ppm; n=23).

276 Sodium shows a positive correlation with $\sum\text{REE}+\text{Y}$ (Fig. 7a), and a negative correlation with the Eu anomaly (Fig. 7b). The
277 Na content is higher in scheelite from deposits hosted in felsic to intermediate rocks (median 120 ppm and 194 ppm,
278 respectively), and lower in deposits hosted in sedimentary rocks (median 53 ppm). Sodium in scheelite from deposits hosted
279 in mafic to ultramafic rocks plots across the range of Na values (4-379 ppm; Fig. 7e).

280 **Vanadium, niobium, tantalum and arsenic**

281 Vanadium, Nb, Ta and As have low concentration in scheelite from orogenic gold deposits with medians of 0.42 ppm, 8.41
282 ppm, 0.13 ppm and 11 ppm, respectively. At Crusader, V, Nb, Ta and As are higher in concentration in the dark CL zone
283 compared to the lighter CL zone (ESM 3d). Niobium and Ta show a positive correlation in all deposits (Fig. 7c).
284 Niobium+Ta+V contents display a positive covariation with REE+Y, forming two broad sub-parallel arrays, with an array for
285 deposits hosted in low and moderate metamorphic facies rocks at lower Na+Ta+V values compared to deposits hosted in high
286 metamorphic facies rocks. In the binary diagram $(\text{Sr}+\text{Na}) / (\text{Sr}+\text{Na}+10\times(\text{Nb}+\text{Ta}+\text{V}+\text{As}))$ vs. $((\text{REE}+\text{Y})+10\times(\text{Nb}+\text{Ta}+\text{V}+\text{As}))$
287 $/ (\text{Sr}+(\text{REE}+\text{Y})+10\times(\text{Nb}+\text{Ta}+\text{V}+\text{As}))$, scheelite from deposits hosted in low to moderate metamorphic facies rocks plots along
288 a vertical trend at $(\text{Sr}+\text{Na})/(\text{Sr}+\text{Na}+10\times(\text{Nb}+\text{Ta}+\text{V}+\text{As})) \sim 1$ (Fig. 9a). Scheelite from deposits hosted in rocks at high
289 metamorphic grade plot typically along a curve from upper left to lower right corners of the diagram (Fig. 9a).

290 **Magnesium, manganese and iron**

291 Correlated peaks in Mg, Mn and Fe, that do not show peaks in Si and S, in LA-ICP-MS spectra indicate
292 submicroscopic inclusions, perhaps oxides. Other inclusions contain Si or S suggesting silicates and sulfides. In scheelite, Mg
293 and Fe are highly correlated ($r^2= 1$), whereas, Mn shows wide covariation with Mg or Fe. Scheelite from deposits hosted in
294 clastic sedimentary rocks has higher Fe and Mg concentrations (~ 29 ppm and ~ 14.8 ppm, respectively) than scheelite from
295 deposits hosted felsic to intermediate rocks (median Fe 23 ppm and 22 ppm, respectively; median Mg 5 ppm and 8 ppm).
296 Iron, Mg and Mn contents are not distinctive for deposits hosted in mafic to ultramafic rocks. The ternary Fe-Mn-Mg diagram
297 (Fig. 9b) shows that scheelite from deposits hosted in low to moderate metamorphic facies rocks have higher Mg, Fe and Mn
298 contents (median Mg 6.5 ppm and 8.6 ppm, respectively; median Fe 27.7 ppm and 26.4 ppm, respectively; median Mn 2.9
299 ppm and 3.4 ppm, respectively), compared to scheelite in deposits hosted in high metamorphic facies rocks (5.4 ppm, ~ 22
300 ppm and 9 ppm, respectively; Fig. 9b). A similar distribution of Fe-Mn-Mg is found for carbonates associated with scheelite,
301 with the exception of the high metamorphic facies Transvaal deposit, which has low Mn and high Mg (Fig. 9c).

302 **Uranium and thorium**

303 Scheelite from deposits hosted in Proterozoic and Phanerozoic rocks have higher Th (median 0.94 ppm and 0.85
304 ppm, respectively) and U (median 4.87 ppm and 1.21 ppm, respectively) concentrations compared to scheelite from deposits
305 hosted in Archean rocks (median Th 0.02 ppm and U 0.02 ppm; Fig. 7i). Thorium and U contents are higher in scheelite from
306 deposits hosted in sedimentary rocks (median 0.88 ppm and 1.8 ppm, respectively), and lower in scheelite from deposits
307 hosted in intermediate plutonic rocks (median 0.01 ppm and 0.01 ppm, respectively). Scheelite from Kochkar has the highest
308 concentrations in Th and U (median 0.98 ppm and 0.6 ppm, respectively). Scheelite from deposits hosted in mafic to ultramafic
309 rocks have Th and U concentrations similar to values for the other deposits (0-1.50 ppm and 0-8.90 ppm, respectively). There
310 is no systematic change in U and Th contents with increasing metamorphic grade of host rocks.

311 **Multivariate statistics of scheelite trace element composition**

312 Principal Component Analysis and PLS-DA of scheelite LA-ICP-MS data (Na, Mg, S, Ti, V, Mn, Fe, Co, As, Sr, Y, Nb, Mo,
313 Ba, Σ REE, Eu anomaly (Eu*), Ta, Pb, Th and U) for orogenic gold deposits are used to investigate the relations between
314 composition and age of mineralization, host rock composition, and metamorphic facies of the host rocks (Fig. 10 and ESM
315 3g). Scheelite from Nevoria has controversial affinity and a trace element composition different to that from the other orogenic
316 gold deposits. For this reason, scheelite from Nevoria is not included from the PLS-DA (Fig. 10). The REE suite has been
317 reduced to Σ REE to facilitate the discussion and emphasize other trace element variations without changing the PCA and
318 PLS-DA results significantly. Data from the Crusader deposit were excluded from both analyses because of its controversial
319 origin, and because it has distinct geochemical features compared to the other orogenic gold deposits. The principal
320 components PC1, PC2 and PC3 represent 20.4 %, 14.1 % and 10.2 %, respectively, of the total variance of the dataset (ESM
321 3g). PC1 is defined by positive contributions of Nb, Σ REE, Y, As, Ta, V and Na (loading > 0.2) and negative contributions
322 of Eu*, Sr, U, Th, Fe, Mg and Ba (loading < -0.2), in decreasing order of importance. PC2 is defined by positive contributions
323 of K, Na, Cu, Zn, Pb, Σ REE, B and Y (loading > 0.2) and negative contributions of Th, U and As (loading < -0.2). PC3 is
324 defined by positive contributions of Mn, Eu*, S, K, Ta and Zn (loading > 0.2) and negative contributions of Σ REE, Mg, Ti,
325 Co, Y and Na (loading < -0.2). In PC1-PC2 and PC1-PC3 spaces (ESM 3g), scheelite from deposits formed during the
326 Proterozoic and Phanerozoic, with the exception of Meliadine (Canada), forms two groups, both with negative PC1 scores.
327 Scheelite from Proterozoic deposits has PC2 and PC3 scores close to 0, whereas, those from Phanerozoic deposits has negative
328 PC2 and PC3 scores. In PC2-PC3 space (ESM 3g), scheelite from Meliadine plots with the Proterozoic deposits, forming a
329 steep array. Scheelite from Archean deposits overlap with that from Proterozoic and Phanerozoic deposits in PC1-PC2, PC1-
330 PC3 and PC2-PC3 spaces (ESM 3g). PLS-DA classifies scheelite by age of mineralization (Fig. 10a and b). Archean deposits

331 are characterized by positive t_1 (positive contributions of Cu, Y, Na and $\sum\text{REE}$) and Proterozoic deposits by negative t_1 and
332 t_2 values (negative contributions of Pb, Zn, Eu*, U), whereas, Phanerozoic deposits have negative t_1 and positive t_2 values
333 (positive contributions of Ba, Mo, As, Mg).

334 Scheelite from deposits hosted in sedimentary rocks have negative PC1 scores, and PC2 and PC3 scores near 0 (ESM
335 3g). Scheelite from deposits hosted in felsic to intermediate rocks, with the exception of Kochkar, have positive PC1, positive
336 PC2, and slightly negative PC3 scores. Scheelite from deposits hosted in felsic to intermediate rocks, with the exception of
337 Kochkar, form an array distinct from that of scheelite from deposits hosted in sedimentary rocks in PC1-PC2 and PC1-PC3
338 (ESM 3g). Scheelite from deposits hosted in mafic to ultramafic rocks overlap with that from deposits hosted in sedimentary
339 and felsic to intermediate rocks in PC1-PC2, PC1-PC3 and PC2-PC3 spaces (ESM 3g). PLS-DA yields marginally improved
340 classification of orogenic gold deposit scheelite according to the composition of the host rocks (Fig. 10c and d). Deposits
341 hosted by ultramafic and mafic rocks overlap slightly with deposits hosted in intermediate rocks and mainly with deposits
342 hosted in sedimentary rocks. Deposits hosted by ultramafic and mafic rocks have low t_2 values, defined by Zn, K, S, Eu*, Fe,
343 B and Cu, whereas, deposits hosted by felsic and sedimentary rocks with positive t_1 values (Mo, Th, V, As; Fig. 10d). Deposits
344 hosted by rocks of intermediate compositions are well classified with negative t_1 values defined by Cu, Y, Na, $\sum\text{REE}$ and Mo
345 (Fig. 10c and d).

346 Scheelite from deposits hosted in low and moderate metamorphic grades rocks have positive to negative PC1, mostly
347 positive PC2, and negative PC3 scores. Scheelite from deposits hosted in high grade metamorphic rocks have positive to
348 negative PC1, mostly negative PC2, and positive PC3 scores. Thus, scheelite from deposits hosted in low and moderate
349 metamorphic grades rocks form a group that partly overlaps with scheelite from deposits in high grade metamorphic rocks in
350 PC2-PC3 space (ESM 3g). Classification of scheelite according to the metamorphic grade of the host rocks by PLS-DA yields
351 well separated deposits hosted by high grade metamorphic rocks with positive t_1 values defined by Mn, As, Nb and Ta (Fig.
352 10e and f). Deposits in low grade metamorphic rocks have negative t_1 and t_2 values (Eu*, U, S, Th), whereas, deposits hosted
353 in intermediate grade metamorphic rocks with low t_1 values are not classified by t_2 , overlapping with deposits hosted in low
354 grade metamorphic rocks with negative t_2 (Fig. 10e and f).

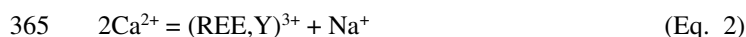
355 Discussion

356 Trace element substitution

357 Cation substitution in scheelite has been discussed for minor elements (Nassau 1963; Nassau and Loiacono 1963;
358 Cottrant 1981; Burt 1989; Raimbault et al. 1993; Brugger et al. 2002; Brugger et al. 2008). Brugger et al. (2008) developed a
359 formal thermodynamic analysis of the controls on $\text{Eu}^{2+}/\text{Eu}^{3+}$ uptake by hydrothermal scheelite. Rare Earth Elements are
360 common in concentrations between 10-5000 ppm in scheelite (Uspensky et al. 1998) and substitute in the Ca site (Raimbault
361 et al. 1993):

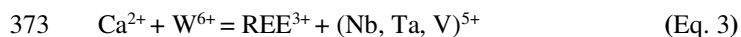


363 The substitution can also be coupled either with Na or Nb to balance the charges (Nassau 1963; Burt 1989; Brugger
364 et al. 2002):



366 The correlation between $\sum\text{REE}+\text{Y}$ and Na (Fig. 7a) is indicative of the coupled substitution mentioned in Eq. 2
367 (Nassau 1963; Nassau and Loiacono 1963; Cottrant 1981; Burt 1989; Raimbault et al. 1993; Brugger et al. 2002). The coupled
368 substitution from Eq. 2 is considered a major substitution in scheelite (Nassau and Loiacono 1963; Cottrant 1981; Burt 1989;
369 Raimbault et al. 1993; Brugger et al. 2002).

370 Octohedral 6-coordinated Ta (V) and V (V) have similar radius (Ta: 78 pm, V: 68 pm) to Nb (78 pm). This, combined
371 with the positive correlation between $\sum\text{REE}+\text{Y}$ and Nb+Ta+V (Fig. 7g) and Eq. 2, suggest that Ta and V may substitute for
372 W in the following coupled substitution such as:



374 The ionic radius of some elements, such as Fe (II, 106 pm), Pb (II, 143 pm) and Mn (II, 110 pm) differ by less than
375 15 %, in 8-coordination, with that of ionic radius of Ca (II) of 126 pm. This suggests that the following substitutions are
376 permissive:



378 In contrast Ba (II, 156 pm) and Mg (II, 103 pm) have more than 15 % difference with Ca^{2+} 8-coordination ionic
379 radius, which perhaps explains the low Ba content in scheelite.

380 The trace element composition of scheelite depends on several factors including the hydrothermal fluid composition,
381 host rock composition, temperature, pressure, pH and Eh, as well as, the partition coefficients between fluid, scheelite, and
382 co-precipitating minerals. The auriferous hydrothermal fluids forming orogenic gold deposits are mixed aqueous-carbonic
383 fluid with a low salinity with a low variance in composition (Goldfarb et al. 2005). Garofalo et al. (2014) showed that the
384 fluids contain Na, subordinate K and B, and minor amounts of trace elements including Cu, As, Li, Sr, Rb, Ba, Cs, Sb and
385 Au. Calcium is absent on this list, consistent with fluid inclusion data as reviewed in Goldfarb et al. (2005), and despite
386 common formation of calcium carbonates (calcite, ankerite) and tungstate (scheelite) in the veins. The low variance in
387 hydrothermal orogenic gold deposit fluid compositions is in contrast to the variations measured in the trace element
388 composition of scheelite, which varies with the metamorphic facies and the host rock composition (Fig. 7, 9 and 10).

389 Manganese concentration in scheelite is lower in low to moderate grade metamorphic rocks, whereas it is higher in
390 deposits hosted in high grade metamorphic rocks (Fig. 9b, 10e). A similar trend is observed for Mn concentrations in
391 carbonates: low to moderate Mn concentration is characteristic for deposits in low and moderate grade metamorphic rocks,
392 whereas moderate to high Mn concentrations are typical for deposits hosted in high grade metamorphic rocks, with the
393 exception of Transvaal (Fig. 9c; ESM 3c). An experimental study of phase transitions of Ca-Mn carbonates by Shi et al.
394 (2012) shows an increase in concentration of MnCO_3 in carbonates with increased pressure, which is consistent with the Mn-
395 rich carbonates in deposits hosted by high grade metamorphic rocks (Fig. 9c). We suggest that the increased Mn contents in
396 scheelite hosted in high grade metamorphic rocks, similarly, may be pressure-related.

397 **Age and host rock composition**

398 The progressive increase of Sr concentration in scheelite from deposits formed during the Archean to the Phanerozoic
399 (Fig. 7d and e) mimics the enrichment in Sr in shales during the Earth cratonization (Condie 1993). Thus, it is likely that the
400 Sr content in scheelite is largely inherited from Sr concentrations in the host rocks. This result corroborates with those of
401 Brugger et al. (2002) who showed that Sr in scheelite from the Mt. Charlotte orogenic gold deposit is partly derived from the
402 felsic units in the host rocks. Brugger et al. (2002) also suggested that Mt. Charlotte scheelite Nd and Pb were derived either
403 locally or regionally from the greenstone belt host rocks. Scheelite from deposits hosted in sedimentary rocks commonly has
404 high concentrations in Pb, U and Th, also shown by Scanlan et al. (2018), compared to scheelite from deposits hosted in other
405 rock types (Fig. 7f and i). Shales commonly have high Pb, U and Th compared to other rock types (Condie 1993), which
406 suggests that a Pb, U and Th signature in scheelite is also inherited from the sedimentary host rocks. This corroborates the
407 results of Mortensen et al. (2010) who showed the Pb isotope compositions of sulfides are similar to those from the
408 sedimentary rocks that host the gold mineralization in the Otago Schist (New Zealand). Scheelite from deposits hosted in

409 sedimentary and felsic to intermediate rocks, with the exception of Kochkar, plot as two groups in PC1-PC2 and PC1-PC3
410 spaces (ESM 3g), and in t_1 - t_2 (Fig. 10d), indicating that the host rock compositions exert a control on the fluid trace element
411 composition, likely as a result of the reaction and exchange between hydrothermal fluids and host rocks, a well-documented
412 process (Ridley and Diamond 2000; Goldfarb et al. 2005; Goldfarb and Groves 2015). Overlap of scheelite compositions,
413 classified by host rock types (Fig. 10d), likely reflects the complex lithological packages hosting the deposits, compared to
414 the simplified lithological classification used in our PLS-DA. For example, the Cuiaba deposit is attributed to the mafic
415 volcanic host rock class because this is the dominant lithology, but the lithological package also comprises Fe-carbonate facies
416 BIF, perhaps explaining the PC1-PC2 scores overlapping the sedimentary and mafic volcanic class fields (ESM 3g). The
417 Meliadine deposit represents an interesting case documenting the influence of the host rock composition on the geochemistry
418 of scheelite. Meliadine is hosted by Archean rocks, but mineralization is Proterozoic in age (Lawley et al. 2015). This could
419 explain why Meliadine scheelite plots with Archean deposits in PC1-PC2 space (ESM 3g) and when projected on t_1 - t_2 (Fig.
420 10b), thus suggesting that the composition is determined, at least in part, by secular change in composition of the cratonic
421 host rocks.

422 Chemical elements that are important in classification of orogenic gold deposits by dominant host rock lithology
423 likely were leached by hydrothermal fluids from the regional country rocks. These elements (Fig. 10) are Sr, Ba, Th, U in
424 sedimentary rock-hosted, Mo in felsic rock-hosted, Cu, Na, Σ REE, Y in intermediate rock-hosted, and Eu*, Fe, K, S, Zn in
425 mafic rock-hosted deposits, whereas ultramafic-rock hosted deposits plot near the origin of the loadings biplot indicating
426 lesser quality classification (Fig. 10c). In contrast, some elements (Co, Mg, Pb, Ti) consistently have low VIP values in
427 classifying orogenic gold deposits with respect to the dominant host rock lithology. Some of these elements (Co, Ti) have a
428 low solubility in hydrothermal fluids and their concentrations could be less modified by exchange with the country rocks, but
429 this is not the case for Mg and Pb, as shown by the variation in Pb isotope composition in scheelite (Brugger et al. 2002).

430 **REE patterns**

431 A comparison of scheelite REE patterns with those of the host rocks from the deposits (ESM 3e and f) shows no systematic
432 trend. This is in agreement with Brugger et al. (2000b) and Brugger et al. (2002) who showed that scheelite exerts a strong
433 crystallographic control on the REE incorporation. Brugger et al. (2008) advocated closed-system crystallization of scheelite
434 to explain the change in REE patterns at Mt. Charlotte. The various REE patterns in orogenic gold deposits are not commonly
435 found in the same grains, such that a closed-system process is not applicable to most scheelite from orogenic gold deposits.
436 Scheelite has REE patterns similar to those of the country rocks at Kochkar, Kumtor, Hollinger and Mt. Charlotte (Kerrich

437 and Fryer 1978; Condie 1993; Kolb et al. 2005; Mueller 2015), which may indicate a local source for the REE, or that the
438 host rocks are equivalents of the source rocks, but just at different crustal depths. In other deposits (Meliadine, Sigma,
439 Lamaque, Young Davidson, and Crusader), scheelite REE patterns differ from those of host rocks, perhaps indicating that the
440 REE signature was not acquired by simple exchange with local country rocks for which the REE patterns are known. The
441 various REE patterns in scheelite do not correlate with the metamorphic grade of the host rocks, consistent with lack of change
442 of REE patterns of rocks during prograde metamorphism (Spandler et al. 2003). The range of REE patterns in scheelite
443 suggests that REE fluid-scheelite partitioning is not the dominant process controlling scheelite composition, but, instead, that
444 the REE patterns are controlled by the composition of hydrothermal fluids (Sylvester and Ghaderi 1997; Ghaderi et al. 1999;
445 Brugger et al. 2000b; Dostal et al. 2009; Peng et al. 2010; Song et al. 2014) and, perhaps, the partition coefficient of co-
446 precipitating minerals, although we do not have adequate data to discuss this hypothesis. For instance, Song et al. (2014) and
447 Zhao et al. (2018) assumed, based on the HREE enriched patterns in garnet and amphibole, that the LREE enriched patterns
448 in skarn scheelite resulted from crystallization garnet and amphibole, which left the residual fluid depleted in HREE.
449 Similarly, Cave et al. (2016) suggested that early crystallization of epidote, titanite and apatite, which have LREE enriched
450 patterns, may be responsible for the HREE enriched patterns in syn-metamorphic scheelite from the orogenic gold deposits
451 of the Otago Schist (New Zealand). The fact that the gold-bearing hydrothermal fluids display limited compositional variation
452 between orogenic gold provinces (Goldfarb et al. 2005), suggests that the variation in REE patterns in scheelite reflects the
453 sources of hydrothermal fluids with some modifications by reaction with the deposit country rocks.

454 The flat and bell-shaped patterns have previously recognized at Drysdale, Mt. Charlotte (Brugger et al. 2000a;
455 Brugger et al. 2000b), Björkdal (Roberts et al. 2006), and the Kambalda and Norseman districts (Ghaderi et al. 1999). Both
456 patterns are found in several additional orogenic gold deposits, which suggests similar fluid sources or similar fluid
457 compositions (ESM 3e and f). Several studies showed that scheelite from orogenic-gold deposits can exhibit two REE patterns
458 in one grain, more commonly evolving from a bell-shaped pattern to a flat and MREE-depleted pattern, with positive Eu
459 anomalies (Sylvester and Ghaderi, 1997; Ghaderi et al., 1999; Brugger et al., 2000). Brugger et al. (2000a; 2002) showed that
460 subtle CL zoning in Mt. Charlotte scheelite correlates with a change from a bell-shaped to a flat REE pattern and interpreted
461 that change as varying amounts of REE fractionated by scheelite crystallisation in closed system reflecting the dynamics of
462 the hydrothermal system. A change in REE patterns from flat to bell-shaped, associated with CL zoning, is also documented
463 at Macraes and Mt Pleasant (Fig. 2e and 3). The flat and bell-shaped REE patterns are commonly found in the same deposit
464 or in the same scheelite grain (Fig. 5 and ESM 3e and f). At Macraes, the flat pattern predates the bell-shaped pattern, which

465 suggests a change in fluid composition between the two scheelite stages (Dostal et al. 2009; Ghaderi et al. 1999; Brugger et
466 al. 2000b).

467 Scheelite in the Kochkar, Kumtor and Muruntau (first generation scheelite, Kempe et al. 2001) orogenic gold deposits
468 have LREE-enriched patterns, and yet are hosted in different rock types in different tectonic terranes (Mao et al. 2004; Kolb
469 et al. 2005). The scheelite REE patterns from each of these deposit share similarities with the REE pattern of their respective
470 host rock (ESM 3e and f; Kempe et al. 2001). The Kumtor scheelite REE pattern, hosted in carbonaceous phyllite and
471 diamictite (Mao et al. 2004) is similar to those of Phanerozoic shales (ESM 3e; Condie 1993). Based on Sr, Sm and Nd isotope
472 compositions at Muruntau, Kempe et al. (2001) concluded that the most probable source of Sr and Nd in both generations of
473 scheelite (LREE-enriched and bell-shaped patterns) was from the metasedimentary host rocks through intensive fluid-rock
474 exchange.

475 The Crusader and Hutti deposits have HREE-enriched patterns (Fig. 5e) similar to that of syn-metamorphic scheelite
476 from the Otago schist (Type-A scheelite; Cave et al. 2016). The positive-slope REE pattern at Hutti (Type II in stage 2
477 scheelite) has been interpreted to be derived from a different hydrothermal event, at a different temperature and pressure, than
478 scheelite with the bell-shape pattern (Hazarika et al. 2016). Cave et al. (2016) explained the Otago schists scheelite HREE-
479 enriched patterns by partitioning of LREE in the co-precipitating Ca-rich silicates.

480 **Eu anomaly**

481 The incorporation of REE³⁺ in scheelite is controlled by coupled substitutions, whereas Eu²⁺ can substitute directly
482 for Ca in scheelite (eq. 4; Nassau 1963; Nassau and Loiacono 1963; Cottrant 1981; Burt 1989; Raimbault et al. 1993; Ghaderi
483 et al. 1999; Brugger et al. 2008). The most important factors controlling the Eu anomaly include: initial Eu²⁺/Eu³⁺ ratio in
484 hydrothermal fluid, redox state, temperature, as well as the relative abundance of sites for Eu²⁺ and Eu³⁺ substitution in the
485 structure of scheelite (Ghaderi et al. 1999). High abundance of Eu²⁺ may also derive from feldspar alteration by hydrothermal
486 fluids (Alderton et al. 1980).

487 Strong positive Eu anomalies are predominantly associated with flat REE patterns that have low \sum REE content,
488 whereas, weak positive to negative Eu anomalies are characteristic of scheelite with higher \sum REE content (Fig. 5 and 6b).
489 Similar to Ghaderi et al. (1999), some deposits hosted in greenschist facies rocks display small variations of the magnitude of
490 the positive Eu anomaly associated with a variation in the concentrations of the other REE (e.g. Essakane, Paddington,
491 Macraes; ESM 3e and f). However, some deposits hosted in moderate to high grade metamorphic rocks show large variations
492 of the size of the Eu anomaly associated with small variations of Eu concentrations (e.g. Tarmoola, Marvel Loch, Norseman,
493 Mt. Charlotte; ESM 3f). In the Kalgoorlie-Norseman region, Ghaderi et al. (1999) proposed that at greenschist facies, high

494 Na activity was caused by buffering of the fluids by mafic rocks, whereas low Na activity is characteristic of high metamorphic
495 grades. However, as shown on Figure 7b, the increase in scheelite Na concentrations correlates with a change from a strong
496 positive to a negative Eu anomaly, but it does not correlate with a change in metamorphic grade. The high Na concentration
497 associated with negative Eu anomaly in scheelite is characteristic of deposits hosted by felsic to intermediate host rocks (Fig.
498 7b; e.g. Young Davidson, Beaufor, Sigma, Lamaque, Canadian Malartic), which suggests that high Na concentrations in
499 hydrothermal fluids precipitating scheelite may be due to fluid exchange with Eu-poor albite.

500 Based on the metamorphic grade of host rocks, and estimated P-T conditions of gold mineralization (ESM 1), Eu
501 should occur predominantly in the divalent state (>250°C, Sverjensky 1984; Liu et al. 2017) in deposits hosted in moderate
502 and high grade metamorphic rocks. However, the P-T conditions of hydrothermal fluids from which scheelite crystallized are
503 not well constrained for all the studied deposits. Therefore, Eu^{3+} may be dominant in deposits formed at the lower end of
504 temperatures recorded for orogenic gold deposits. In addition, Brugger et al. (2008) showed that the $\text{Eu}^{2+}/\text{Eu}^{3+}$ ratio is
505 controlled by pH, whereas, Liu et al. (2017) showed the aqueous species have a significant impact on the oxydation state of
506 Eu in hydrothermal fluids. As mentioned above, various mechanisms such as direct substitution of Eu^{2+} for Ca and coupled
507 substitutions of Eu^{3+} may also affect $\text{Eu}^{3+}/\text{Eu}^{2+}$ ratios in REE patterns of scheelite. In addition to the temperature dependence
508 of $\text{Eu}^{3+}/\text{Eu}^{2+}$ ratios (Sverjensky 1984), high Na concentrations associated with variations in the Eu anomaly (Fig. 7b), support
509 the work of Brugger et al. (2008) that suggested the coupled substitution $2\text{Ca}^{2+} = \text{REE}^{3+} + \text{Na}^{+}$ plays an important role
510 controlling REE^{3+} substitution during scheelite crystallization from hydrothermal fluids.

511 **Comparison to scheelite from other types of deposits**

512 **Trace element composition**

513 Previous studies show that scheelite from several orogenic gold deposit have similar $(\text{Gd}/\text{Yb})_{\text{CN}}$ and $(\text{La}/\text{Sm})_{\text{CN}}$ ratios
514 (Fig. 6a) and similar $\sum\text{REE}$ and Eu anomaly (Fig. 6b) to those reported in our study. Scheelite from other gold, porphyry-
515 related, breccia, greisen, skarn and polymetallic vein deposits have similar $(\text{Gd}/\text{Yb})_{\text{CN}}$ and $(\text{La}/\text{Sm})_{\text{CN}}$ ratios (Fig. 6c) and
516 similar $\sum\text{REE}$ and Eu anomaly (Fig. 6d) compared to scheelite from orogenic gold deposits. Thus, the REE patterns including
517 the $(\text{Gd}/\text{Yb})_{\text{CN}}$ and $(\text{La}/\text{Sm})_{\text{CN}}$ ratios, $\sum\text{REE}$ and the Eu anomaly do not discriminate orogenic gold deposit scheelite from that
518 from other types of deposits. Scheelite from orogenic gold deposits commonly have high Sr content, high Sr/Mo ratio, large
519 Eu anomaly, and low Mo and As contents compared to scheelite from other deposit types (Fig. 11), such that Sr, Mo, and As,
520 combined with the Eu anomaly are useful to distinguish orogenic gold deposit scheelite from that from other types of mineral
521 deposits.

522 Strontium, Mo, Y and the REE, with the exception of Lu, are used in PCA and PLS-DA of orogenic gold deposit
523 scheelite against other types of deposits including gold, skarn, porphyry-related, greisen, breccia and polymetallic veins (Fig.
524 12 and ESM 3h). These elements were selected for the PCA and the PLS-DA, because they are more commonly reported.
525 The PCA yields PC1 with 56.0 %, PC2 with 19.4 % and PC3 with 11.4 % of the total variance (ESM 3h). PC1 is defined by
526 high positive contributions of the HREE including Gd, Tb, Dy, Ho, Er, Tm, Yb and Y, and high negative contributions of the
527 LREE including La, Ce, Pr and Nd. PC2 shows similar variation than PC1 and is defined by high negative contributions of
528 the HREE and Y and high positive contributions of the LREE. PC3 is defined by high positive contributions of Eu and Sr and
529 high negative contribution of Mo. Orogenic gold deposit scheelite has PC1 scores more similar to those from the other deposit
530 types (ESM 3h). Orogenic gold deposit scheelite commonly has positive PC3 scores, whereas scheelite from the other deposit
531 types commonly has negative PC3 scores. Thus, the PC1-PC3 space allows orogenic gold deposit scheelite to be distinguished
532 from scheelite from other deposit types (ESM 3ESM 3h). In the PC1-PC3 space, scheelite from Kochkar, Kumtor, Canadian
533 Malartic and Nevoria forms an intermediate group and overlaps with some greisen, skarn and polymetallic vein scheelite
534 (ESM 3h). Using PLS-DA (Fig. 12), qw^*_1 is defined by positive contributions of Mo, La, Ce and Pr, and negative contributions
535 of Y, Sr and Eu, Gd, Tb, Dy, Ho, Er and Tm, whereas qw^*_2 is defined by positive contributions of Mo and negative
536 contributions of Sr and Eu. Orogenic gold deposit scheelite has positive Eu and Sr, and negative Mo, contributions. Scheelite
537 from other types of deposits commonly has negative contributions of Eu and Sr, and positive contributions of Mo. The qw^*_1 -
538 qw^*_2 loadings display distinct trace element compositions between orogenic gold deposit scheelite and that from the other
539 deposit types, which causes the sharp separation in t_1 - t_2 space (Fig. 12). Strontium, Mo and Eu commonly have VIP greater
540 than 1 for each class (Fig. 12c), which shows that they are the main elements that contribute to deposit type discrimination.
541 On the other hand, REE and Y commonly have VIP lower than 0.8 (Fig. 12c), which shows that they do not contribute
542 significantly to deposit type discrimination. A combination of binary plots (Fig. 11), PCA (ESM 3ESM 3h), and PLS-DA
543 (Fig. 12), thus shows that the main elements that discriminate scheelite from orogenic gold deposits from that from other
544 deposit types are Sr, Mo, As and Eu. PCA and PLS-DA, combined with $(Gd/Yb)_{CN}$ vs $(La/Sm)_{CN}$ and $\sum REE$ vs Eu^* , show
545 that REE are not discriminant for orogenic gold deposit scheelite compared to that from the other deposit types. We conclude
546 that trace elements Sr, Mo, As, and Eu have high potential to discriminate orogenic gold deposit scheelite from that from
547 other deposit types. Thus, scheelite trace element composition has potential to orient exploration using indicator mineral
548 surveys. However, trace element data other than REE are not well characterized in scheelite from other deposit types, which
549 constrains the number of discriminant elements that can be studied here.

550 Nevoria has been ascribed to the orogenic gold deposit type by several authors (Eilu et al. 1999; Goldfarb et al. 2005)
551 but skarn by others (Mueller 1997; Mueller et al. 2004). Scheelite from the Nevoria gold deposit shows a different trace

552 element composition compared to scheelite from the other orogenic gold deposits including yellowish UVC colour, high Mo
553 concentration (Figs 8 and 11), low Sr/Mo ratio (Fig. 11), and a flat REE pattern without an Eu anomaly (Fig. 5). Scheelite
554 from Nevoria plot within the field associated with the other deposit types in PLS-DA (Fig. 12) and PCA (ESM 3h). This
555 shows that Nevoria's scheelite has a composition with a skarn affinity, consistent with the interpretation of Mueller 1997;
556 Mueller et al. 2004), providing a proof of concept for the scheelite chemical discrimination method.

557 **Conclusions**

558 Orogenic gold deposit scheelite is typically homogeneous in CL and exhibits a blue colour under short wave UVC
559 light, a characteristic of Mo-poor scheelite. Scheelite exhibits rare sector or oscillatory zoning and breccia texture that indicate
560 precipitation from hydrothermal fluids with different trace element compositions. Rare earth elements display five patterns
561 with a scheelite/chondrite average ratio near 100: a bell-shaped pattern with a i) positive or ii) negative Eu anomaly, iii) a flat
562 pattern with a positive Eu anomaly, and less commonly iv) a LREE-enriched pattern, and v) a HREE-enriched pattern. The
563 variation of REE patterns in scheelite suggests that scheelite-fluid REE fractionation is not the dominant processes controlling
564 scheelite composition, but, instead, that REE patterns are most probably controlled by the source of the hydrothermal fluid.
565 The bell-shaped and flat patterns are found in most of the orogenic gold deposits suggesting fluids with similar chemistry,
566 due to similar sources for the hydrothermal fluids. The Eu anomaly likely reflects the temperature of scheelite crystallization,
567 the substitution mechanism and the Na activity during crystallization. Scheelite from deposits hosted in low and moderate
568 metamorphic facies rocks commonly have high $\sum\text{REE}+\text{Y}$, Sr and Na, and low Mn and Nb+Ta+V contents, whereas scheelite
569 from deposits hosted in high metamorphic facies rocks commonly have low $\sum\text{REE}+\text{Y}$, Sr and Na, and high Mn and Nb+Ta+V
570 contents. The binary diagram $(\text{Sr}+\text{Na})/(\text{Sr}+\text{Na}+10\text{x}(\text{Nb}+\text{Ta}+\text{V}+\text{As}))$ vs.
571 $((\text{REE}+\text{Y})+10\text{x}(\text{Nb}+\text{Ta}+\text{V}+\text{As}))/(\text{Sr}+(\text{REE}+\text{Y})+10\text{x}(\text{Nb}+\text{Ta}+\text{V}+\text{As}))$ enables scheelite from deposits hosted in low and
572 moderate metamorphic facies to be differentiated from scheelite from deposits hosted in high metamorphic facies rocks. As
573 well, PLS-DA allows scheelite from deposits hosted in low and moderate metamorphic facies rocks to be separated from
574 those from deposits hosted in high metamorphic facies rocks (Fig. 10e and f). Scheelite from deposits hosted in felsic to
575 intermediate rocks commonly have high $\sum\text{REE}$, Y and Na, and low Pb, Sr, U and Th concentrations, and a negative Eu
576 anomaly, whereas, scheelite from deposits hosted in sedimentary rocks have low $\sum\text{REE}$, Y and Na, and typically high Pb, Sr,
577 U and Th concentrations. PLS-DA separates scheelite from deposits hosted in felsic to intermediate rocks from that from
578 deposits hosted in sedimentary rocks. Both groups overlap partially with scheelite from deposits hosted in mafic-ultramafic
579 rocks. The overlap likely reflects the complex lithological packages hosting the deposits. Orogenic gold deposit scheelite REE

580 patterns cannot be distinguished from those of scheelite from other deposit types. Trace element composition, PCA, and PLS-
581 DA show a distinct trace element signatures in Sr, Mo, Eu, As and Sr/Mo for orogenic gold deposit scheelite, compared to
582 scheelite from other deposit types.

583 **Acknowledgements**

584 The research is funded by Agnico Eagle Mines Ltd, the Ministère de l'Énergie et des Ressources Naturelles du
585 Québec and the Natural Sciences and Engineering Research Council. People and mining companies who collaborated are
586 gratefully thanked: Acacia Mining, AngloGold Ashanti, D. Craw (Otago University), C. Daoust, A. Dziggel (Aachen
587 University), Goldcorp, S. Hagemann (UWA), A. Hellmann (Aachen University), IAMgold, R. Large (University of
588 Tasmania), L. M. Lobato (Universidade Federal de Minas Gerais), N. Maneglia (Université Laval), A. Mueller (UWA), F.
589 Robert (Barrick), Royal Ontario Museum, N. Thébaud (UWA). M. Choquette (Université Laval), D. Savard and M. Kudrna
590 Prasek (UQAC) are thanked for the technical assistance with EPMA and LA-ICP-MS analyses. Roman Hanes is thanked for
591 his help to elaborate the discussion. We thank the reviewers and Editor B. Lehmann for their insightful comments that help
592 improve our contribution significantly.

593 **Figures captions**

594 Fig. 1. Scheelite texture and mineral associations in orogenic gold deposits **a** aggregate of anhedral scheelite grains (Cuiaba,
595 Brazil), **b** subhedral scheelite grains (Canadian Malartic, Abitibi), **c** dynamic recrystallization of scheelite at Hutti (India), **d**
596 fine grains disseminated scheelite (Kochkar, Russia), **e** scheelite veins (Kumtor, Kyrgyzstan), **f** scheelite associated with
597 hydrothermal and metamorphic minerals such as clinopyroxene (Navachab, Namibia), **g** scheelite in association with
598 tourmaline (Essakane, Burkina Faso), **h** scheelite is associated with pyrite with gold inclusion at Tarmoola, Eastern Goldfields,
599 **i** scheelite with native gold, magnetite and hematite (Crusader, Australia).

600 Fig. 2. Cathodoluminescence (CL) images of scheelite show **a** homogeneous CL (Dome, Abitibi; the halo effect is an artefact
601 due to camera resolution), **b** sub-grains within larger scheelite (Essakane, Burkina Faso), **c** homogeneous fine grains (Hutti,
602 India), **d** homogenous scheelite cut by thin veinlets (Tarmoola, Yilgarn), **e** brecciated (Mount Pleasant, Southern Cross) **f**
603 brecciated structure at the edge of the grain (Crusader, Australia), **g** oscillatory zoning (Kochkar, Russia), **h** homogeneous CL
604 (Rosebel, Suriname), **i** oscillatory zoning (Crusader, Agnew district).

605 Fig. 3. Variation of the trace elements composition with the CL zonation in scheelite from the Macraes deposit, New Zealand.
606 **a** The CL shows two generations: the first generation labelled “1” is brecciated by the second generation labelled “2”. **b** LA-
607 ICP-MS profile shows the trace element variation within the different scheelite generations. The first generation is
608 characterized by high Sr, Na, Mg, Mn, Th and U, and low Y and $\sum\text{REE}$ content, whereas, the second generation is
609 characterized by low Sr, Na, Mg, Mn, Th and U, and high Y and $\sum\text{REE}$ content. Zones 2a and 1b are too small to be quantified.
610 **c** The first generation is characterized by a flat REE pattern and the second generation is characterized by a bell-shaped REE
611 pattern, both with positive Eu anomalies.

612 Fig. 4. Images of scheelite **a** reflected light, **b** cathodoluminescence and trace elements LA-ICP-MS maps in **c** Sr, **d** Mo, **e**
613 Na, **f** Y, **g** Nb, **h** As, **i** Eu, **j** Gd and **k** Pb, show homogeneous composition typical for scheelite from orogenic gold deposits
614 (Dome, Abitibi).

615 Fig. 5. Rare earth element patterns in scheelite from orogenic gold deposits. **a** bell-shaped pattern with positive Eu anomaly,
616 **b** flat pattern with positive Eu anomaly, **c** bell-shaped with negative Eu anomaly, **d** LREE-enriched pattern, **e** HREE-enriched
617 pattern, **f** flat pattern without Eu anomaly. Data are normalized to chondrite from McDonough and Sun (1995). The North
618 American Shale Composite (NASC) values are from Gromet et al. (1984).

619 Fig. 6. Binary plots for REE contents in scheelite **a** $(\text{Gd}/\text{Yb})_{\text{CN}}$ vs $(\text{La}/\text{Sm})_{\text{CN}}$ and **b** $\sum\text{REE}$ vs Eu^* from orogenic gold deposits,
620 **c** $(\text{Gd}/\text{Yb})_{\text{CN}}$ vs $(\text{La}/\text{Sm})_{\text{CN}}$ and **d** $\sum\text{REE}$ vs Eu^* from various deposit types. Data for orogenic gold deposits from literature
621 include Ghaderi et al. (1999); Brugger et al. (2000b); Roberts et al. (2006); Xiong et al. (2006); Liu Yan et al. (2007); Dostal
622 et al. (2009); Song et al. (2014); Cave et al. (2016); Hazarika et al. (2016); Poulin (2016). Abbreviations: Bell + : bell-shaped
623 pattern with positive Eu anomaly; Bell - : bell-shaped pattern with negative Eu anomaly; Bell Ho + : bell-shaped pattern
624 centered in Ho with positive Eu anomaly as described in Dostal et al. (2009); Bell Ho - : bell-shaped pattern centered in Ho
625 with negative Eu anomaly as described in Dostal et al. (2009).

626 Fig. 7. LA-ICP-MS trace element binary plots for scheelite from orogenic gold deposits **a** $\sum\text{REE}+\text{Y}$ vs Na; **b** Eu anomaly
627 (Eu^*) vs Na; **c** Nb vs Ta; **d** $\sum\text{REE}+\text{Y}$ vs Sr; **e** Na vs Sr, data for Rosebel are from EPMA; **f** Pb vs Sr; **g** $\sum\text{REE}+\text{Y}$ vs Nb+Ta+V;
628 **h** $\sum\text{REE}$ vs Y; **i** U vs Th. Data from the literature include Ghaderi et al. (1999) and Dostal et al. (2009).

629 Fig. 8. Scheelite composition from orogenic gold and other deposit types for **a** Sr, **b** Mo, **c** Y and **d** Na. Literature data for
630 orogenic gold deposits are from Anglin et al. (1996); Ghaderi et al. (1999); Brugger et al. (2000b); Dostal et al. (2009);
631 Graupner et al. (2010); Hazarika et al. (2016); Poulin 2016; Poulin et al. (2016). Data for skarn deposits are from Eichhorn et

632 al. (1997); Zhigang et al. (1998); Liu Yan et al. (2007); Peng et al. (2010); Song et al. (2014); Poulin (2016); Poulin et al.
633 (2016). Data for Greisen and VMS are from Poulin (2016). Abbreviation: Can. Malartic: Canadian Malartic.

634 Fig. 9. LA-ICP-MS trace element diagrams for scheelite in orogenic gold deposits **a** $(\text{Sr}+\text{Na})/(\text{Sr}+\text{Na}+10\times(\text{Nb}+\text{Ta}+\text{V}+\text{As}))$
635 vs $(\text{REE}+\text{Y}+10\times(\text{Nb}+\text{Ta}+\text{V}+\text{As})) / (\text{Sr}+\text{REE}+\text{Y}+10\times(\text{Nb}+\text{Ta}+\text{V}+\text{As}))$; **b** Fe-Mn-Mg scheelite composition measured by LA-
636 ICP-MS; **c** Fe-Mn-Mg carbonate composition associated with scheelite in orogenic gold deposits, measured by EPMA.

637 Fig. 10. Partial Least Square-Discriminant Analysis of LA-ICP-MS data for scheelite in orogenic gold deposits. **a** $q_{w1}^*-q_{w2}^*$
638 and **b** t_1-t_2 scores for mineralization age; **c** $q_{w1}^*-q_{w2}^*$ and **d** t_1-t_2 scores for host rock compositions; **e** $q_{w1}^*-q_{w2}^*$ and **f** t_1-t_2
639 scores for metamorphic facies of the host rocks. The $q_{w1}^*-q_{w2}^*$ plots show the correlation between elements and the element
640 contribution to each group. The t_1-t_2 plots show the distribution of scheelite sample according to each preselected grouping.

641 Fig. 11. LA-ICP-MS trace element binary plots for scheelite from orogenic gold deposits and other deposit types **a** Sr vs Eu
642 anomaly (Eu^*), **b** Sr/Mo vs Eu^* , **c** Mo vs As, and **d** Sr/Mo vs As. Data for orogenic gold deposits: Ghaderi et al. (1999);
643 Dostal et al. (2009); Cave et al. (2016); Hazarika et al. (2016); Poulin (2016). Data for skarn deposits: Xiong et al. (2006);
644 Ren et al. (2010); Song et al. (2014); Guo et al. (2016); Poulin (2016); Fu et al. (2017), and for porphyry-related deposits:
645 Poulin (2016) and Sun and Chen (2017).

646 Fig. 12. Partial Least Square-Discriminant Analysis of LA-ICP-MS data for scheelite from different deposit types. **a** The
647 $q_{w1}^*-q_{w2}^*$ loadings plot shows correlations among elemental variables and deposit types. **b** The t_1-t_2 scores plot shows the
648 distribution of scheelite samples in the $q_{w1}^*-q_{w2}^*$ space. **c** Variable importance of the projection (VIP) per deposit types
649 shows the detailed element contribution per deposit. Data for orogenic gold deposits: Ghaderi et al. (1999); Dostal et al.
650 (2009); Hazarika et al. (2016) and Poulin (2016), for skarn deposits: Song et al. (2014) and Poulin (2016) and for porphyry-
651 related deposits: Poulin (2016) and Sun and Chen (2017).

652

653

Electronic Supplementary Materials captions

654 ESM 1. (a) Geological settings of the gold deposits; (b) Scheelite characteristics in the studied orogenic gold deposits

655 ESM 2. (a) Analytical conditions for trace element analyses in scheelite by EPMA; (b) EPMA elements composition in
656 scheelite from orogenic gold deposits; (c) Analytical conditions for trace element analyses in scheelite by LA-ICP-MS; (d)
657 LA-ICP-MS trace elements composition in scheelite from orogenic gold deposits

658 ESM 3. (a) Comparison between LA-ICP-MS and EPMA analyses for **a** Sr, **b** Mo, **c** Y and **d** Na. Red line – 1:1 ratio;
659 abbreviation: DL: Detection limit of the electron microprobe; (b) Trace elements concentrations sorted by median scheelite
660 composition for orogenic gold deposits, measured by LA-ICP-MS; (c) Carbonate coloration of samples with scheelite for
661 deposits hosted in **a** low grade metamorphic facies rocks **b** moderate grade metamorphic facies rocks **c** high grade
662 metamorphic facies rocks; (d) Variation of the trace elements composition with **a** the oscillatory zoning shown by CL in
663 scheelite from the Crusader deposit, Agnew district (Australia). Zone 1 is characterized by **a** darker CL and high content in
664 Na, V, As, Nb, Ta, Y and REE, and low Mo in **b**. Zone 2 is brighter CL and low content in Na, V, As, Nb, Ta, Y and REE,
665 and higher Mo. **c** Both zones have a similar positive-slope REE pattern.; (e) Rare earth elements patterns from LA-ICP-MS
666 data in scheelite from **a** Dome and Hollinger (Timmins, Canada); **b** Young Davidson (Matachewan, Canada); **c** Malartic
667 (Canada), **d** Val-d'Or camp (Canada); **e** Meliadine (Canada); **f** Cuiaba (Brazil); **g** Buzwagi (Tanzania) and Essakane (Burkina
668 Faso), **h** Hutti (India); **i** Kochkar (Russia); **j** Kumtor (Kyrgyzstan); (f) Rare earth elements patterns from LA-ICP-MS data in
669 scheelite from **a** Marvel Loch (Australia); **b** Nevoria (Australia); **c** Edward's Find (Australia); **d** Crusader (Australia); **e**
670 Tarmoola (Australia); **f** Paddington (Australia); **g** Mt Pleasant (Australia); **h** Norseman camp (Australia); **i** Mt. Charlotte
671 (Australia); **j** Macraes (New Zealand); (g) Principal Component Analysis of LA-ICP-MS data for scheelite in orogenic gold
672 deposits. Rare Earth Elements are reduced to \sum REE and Eu anomaly (Eu*). **a** PC1-PC2, **b** PC1-PC3 and **c** PC2-PC3 with
673 emphasis on the mineralization age, **d** PC1-PC2, **e** PC1-PC3 and **f** PC2-PC3 with emphasis on the host rock composition, **g**
674 PC1-PC2, **h** PC1-PC3 and **i** PC2-PC3 with emphasis on the metamorphic facies of the host rock; (h) Principal Component
675 Analysis of LA-ICP-MS data for scheelite from different deposit types. Data from the literature for orogenic gold deposits:
676 Dostal et al. (2009); Hazarika et al. (2016) and Poulin (2016), for skarn deposits: Song et al. (2014) and Poulin (2016), and
677 for porphyry related deposits: Poulin (2016) and Sun and Chen (2017).

678

References

679 Alderton DHM, Pearce JA, Potts PJ (1980) Rare earth element mobility during granite alteration; evidence from Southwest
680 England. *Earth Planet Sci Lett* 49:149-165

681 Anglin CD (1992) Sm-Nd and Sr Isotopic Studies of Scheelite From Some Superior Province Gold Deposits Department of
682 Earth Sciences. Carleton University, Ottawa, pp 219

683 Anglin CD, Jonasson IR, Franklin J (1996) Sm-Nd dating of scheelite and tourmaline: Implications for the genesis of Archean
684 gold deposits, Val d'Or, Canada. *Econ Geol* 91:1372-1382

685 Aumo R, Salonen V-P (1986) Uvarovite and glacial transportation distance as provenance indicators of ore mineralization in
686 the southern part of the Outokumpu district, north Karelia, Finland *Prospecting in Areas of Glaciated Terrain*.
687 Institution of Mining and Metallurgy, London, pp 17-23

688 Beaudoin G, Pitre D (2005) Stable isotope geochemistry of the Archean Val-d'Or (Canada) orogenic gold vein field *Miner*
689 *Deposita* 40:59-75

690 Bell K, Anglin CD, Franklin JM (1989) Sm-Nd and Rb-Sr isotope systematics of scheelites: Possible implications for the age
691 and genesis of vein-hosted gold deposits. *Geology* 17:500-509

692 Boutroy E, Dare SAS, Beaudoin G, Barnes S-J, Lightfoot PC (2014) Magnetite composition in Ni-Cu-PGE deposits
693 worldwide: application to mineral exploration. *J Geochem Explor* 145:64-81

694 Brugger J, Giere R, Grobety B, Uspensky E (1998) Scheelite-powellite and paraniite-(Y) from the Fe-Mn deposit at Fianel,
695 Eastern Swiss Alps. *Am Mineral* 83:1100-1110

696 Brugger J, Bettioli AA, Costa S, Lahaye Y, Bateman R, Lambert DD, Jamieson DN (2000a) Mapping REE distribution in
697 scheelite using luminescence. *Mineralogical Magazine* 64:891-903

698 Brugger J, Lahaye Y, Costa S, Lambert D, Bateman R (2000b) Inhomogeneous distribution of REE in scheelite and dynamics
699 of Archean hydrothermal systems (Mt. Charlotte and Drysdale gold deposits, Western Australia). *Contrib Mineral*
700 *Petr* 139:251-264

701 Brugger J, Maas R, Lahaye Y, McRae C, Ghaderi M, Costa S, Lambert D, Bateman R, Prince K (2002) Origins of Nd-Sr-Pb
702 isotopic variations in single scheelite grains from Archean gold deposits, Western Australia. *Chem Geol* 182:203-
703 225

704 Brugger J, Etschmann B, Pownceby M, Liu WH, Grundler P, Brewe D (2008) Oxidation state of europium in scheelite:
705 Tracking fluid-rock interaction in gold deposits. *Chem Geol* 257:26-33

706 Burt DM (1989) Compositional and phase relations among rare earth elements. *Reviews in Mineralogy* 21:259-307

707 Cassidy KF, Bennett JM (1993) Gold mineralisation at the Lady Bountiful Mine, Western Australia; an example of a
708 granitoid-hosted Archean lode gold deposit. *Miner Deposita* 28:388-408

709 Cave BJ, Pitcairn IK, Craw D, Large RR, Thompson JM, Johnson SC (2016) A metamorphic mineral source for tungsten in
710 the turbidite-hosted orogenic gold deposits of the Otago Schist, New Zealand. *Miner Deposita Online*

711 Condie KC (1993) Chemical composition and evolution of the upper continental crust: Contrasting results from surface
712 samples and shales. *Chem Geol* 104:1-37

713 Cottrant J (1981) *Cristallochimie et geochimie des terres rares dans la scheelite: Application à quelques gisements français.*
714 Université Pierre et Marie Curie,

715 Darbyshire DPF, Pitfield PEJ, Campbell SDG (1996) Late Archean and Early Proterozoic gold-tungsten mineralization in the
716 Zimbabwe Archean craton: Rb-Sr and Sm-Nd isotope constraints. *Geology* 24:19-22

717 Dare S, Barnes S-J, Beaudoin G, Méric J, Boutroy E, Potvin-Doucet C (2014) Trace elements in magnetite as petrogenetic
718 indicators. *Miner Deposita* 49:785-796

719 de Iorio M, Ebbels TMD, Stephens DA (2007) *Statistical Techniques in Metabolic Profiling* In: Balding DJ, Bishop MJ,
720 Cannings C (eds) *Handbook of statistical genetics*. 3rd ed edn. John Wiley & Sons, Chichester, England, pp 347-373

721 Dostal J, Kontak D, Chatterjee A (2009) Trace element geochemistry of scheelite and rutile from metatubidite-hosted quartz
722 vein gold deposits, Meguma Terrane, Nova Scotia, Canada: genetic implications. *Miner Petrol* 97:95-109

723 Dupuis C, Beaudoin G (2011) Discriminant diagrams for iron oxide trace element fingerprinting of mineral deposit types.
724 *Miner Deposita* 46:319-335

725 Eichhorn R, Höll R, Jagout E, Schärer U (1997) Dating scheelite stages: A strontium, neodymium, lead approach from the
726 Felhertal tungsten deposit, Central Alps, Austria. *Geochim Cosmochim Acta* 61:5005-5022

727 Eilu PK, Mathison CI, Groves DI, Allardye WJ (1999) *Atlas of alteration assemblages, styles and zoning in orogenic lode-*
728 *gold deposits in a variety of host rock and metamorphic settings.* University of Western Australia, Geology
729 Department and Extension Service, Perth, West. Aust., Australia

730 Fipke CE, Gurney JJ, Moore RO (1995) *Diamond exploration techniques emphasizing indicator mineral geochemistry and*
731 *Canadian examples.* GSC Bull 423

732 Frei R, Nägler TF, Schönberg R, Kramers JD (1998) Re-Os, Sm-Nd, U-Pb, and stepwise lead leaching isotope systematics in
733 shear-zone hosted gold mineralization: genetic tracing and age constraints of crustal hydrothermal activity. *Geochim*
734 *Cosmochim Acta* 62:1925-1936

735 Fu Y, Sun X, Zhou H, Lin H, Jiang L, Yang T (2017) In-situ LA-ICP-MS trace elements analysis of scheelites from the giant
736 Beiya gold-polymetallic deposit in Yunnan Province, Southwest China and its metallogenic implications. *Ore Geol*
737 *Rev* 80:828-837

738 Garofalo PS, Fricker MB, Guenther D, Bersani D, Lottici PP (2014) Physical-chemical properties and metal budget of Au-
739 transporting hydrothermal fluids in orogenic deposits. *Special Publication - Geological Society of London* 402:71-
740 102

741 Ghaderi M, Palin JM, Campbell IH, Sylvester PJ (1999) Rare earth element systematics in scheelite from hydrothermal gold
742 deposits in the Kalgoorlie-Norseman region, Western Australia. *Econ Geol* 94:423-437

743 Goldfarb RJ, Baker T, Dube B, D. I. Groves, C. J. R. Hart, Gosselin P (2005) Distribution, character and genesis of gold
744 deposits in metamorphic terranes In: Hedenquist JW, Thompson JFH, Goldfarb RJ, Richards JP (eds) *Economic*
745 *geology 100th Anniversary volume*. pp 407–450

746 Goldfarb RJ, Groves DI (2015) Orogenic gold; common or evolving fluid and metal sources through time. *Lithos (Oslo)*
747 233:2-26

748 Graupner T, Niedermann S, Rhede D, Kempe U, Seltmann R, Williams C, Klemd R (2010) Multiple sources for mineralizing
749 fluids in the Charmitan gold(-tungsten) mineralization (Uzbekistan). *Miner Deposita* 45:667-682

750 Gromet LP, Dymek RF, Haskin LA, Korotev RL (1984) The "North American shale composite"; its compilation, major and
751 trace element characteristics. *Geochim Cosmochim Acta* 48:2469-2482

752 Guo Z, Li J, Xu X, Song Z, Dong X, Tian J, Yang Y, She H, Xiang A, Kang Y (2016) Sm/Nd dating and REE composition
753 of scheelite for the Honghuaerji scheelite deposit, Inner Mongolia, northeast China. *Lithos (Oslo)* 261:307-321

754 Gurney JJ (1984) A correlation between garnets and diamonds in kimberlites. University of Western Australia

755 Hancock MC, Robertson IG, Booth GW (1990) Paddington gold deposits In: Hughes FE (ed) *Geology of Australian and Papua*
756 *New Guinean Mineral Deposits*. Australasian Institute of Mining and Metallurgy Monograph 14,

757 Hazarika P, Mishra B, Pruseth KL (2016) Scheelite, apatite, calcite and tourmaline compositions from the late Archean Hutti
758 orogenic gold deposit: Implications for analogous two stage ore fluids. *Ore Geol Rev* 72:989-1003

759 Jochum KP, Nohl U, Herwig K, Lammel E, Stoll B, Hofmann AW (2005) GeoReM: A New Geochemical Database for
760 Reference Materials and Isotopic Standards. *Geostand Geoanal Res* 29:333-338

761 Johansson P, Keinänen V, Lehmuspelto P (1986) Geochemical exploration of tungsten in glaciogenic deposits in Soretiaupulju,
762 western Finnish Lapland Prospecting in Areas of Glaciated Terrain. Institution of Mining and Metallurgy, London,
763 pp 61-67

764 Jowitt SM, Cooper K, Squire RJ, Thébaud N, Fisher L, Cas RAF, Pegg I (2014) Geology, mineralogy, and geochemistry of
765 magnetite-associated Au mineralization of the ultramafic–basalt greenstone hosted Crusader Complex, Agnew Gold
766 Camp, Eastern Yilgarn Craton, Western Australia; a Late Archean intrusion-related Au deposit ? *Ore Geol Rev*
767 56:53-72

768 Kempe U, Belyatsky B, Krymsky R, Kremenetsky AA, Ivanov PA (2001) Sm-Nd and Sr isotope systematics of scheelite
769 from the giant Au(-W) deposit Muruntau (Uzbekistan): implications for the age and sources of Au mineralization.
770 Miner Deposita 36:379-392

771 Kent AJR, Campbell IH, McCulloch MT (1995) Sm-Nd systematics of hydrothermal scheelite from the Mount Charlotte
772 Mine, Kalgoorlie, Western Australia; an isotopic link between gold mineralization and komatiites. Econ Geol
773 90:2329-2335

774 Kerrich R, Fryer BJ (1978) Archaean precious-metal hydrothermal systems, Dome Mine, Abitibi greenstone belt; II, REE and
775 oxygen isotope relations. Can J Earth Sci 16:440-458

776 Kolb J, Sindern S, Kisters AFM, Michael Meyer F, Hoernes S, Schneider J (2005) Timing of Uralian orogenic gold
777 mineralization at Kochkar in the evolution of the East Uralian granite-gneiss terrane. Miner Deposita 40:473-491

778 Lindmark B (1977) Till-sampling methods used in exploration for scheelite in Kaustinen, Finland Prospecting in Areas of
779 Glaciated Terrain. Institute of Mining and Metallurgy, Helsinki

780 Liu W, Etschmann B, Migdisov A, Boukhalfa H, Testemale D, Mueller H, Hazemann J-L, Brugger J (2017) Revisiting the
781 hydrothermal geochemistry of europium(II/III) in light of new in situ XAS spectroscopy results. Chem Geol 459:61-
782 74

783 Liu Yan, Deng Jun, Li ChaoFeng, Shi GuangHai, AiLi Z (2007) REE composition in scheelite and scheelite Sm-Nd dating
784 for the Xuebaoding W-Sn-Be deposit in Sichuan. Chin Sci Bull 52:2543-2550

785 MacRae CM, Wilson NC, Brugger J (2009) Quantitative Cathodoluminescence Mapping with Application to a Kalgoorlie
786 Scheelite. Microscopy and Microanalysis 15:222-230

787 Mao J, Konopelko D, Seltmann R, Lehmann B, Chen W, Wang Y, Eklund O, Usabaliev T (2004) Postcollisional age of the
788 Kumtor gold deposit and timing of Hercynian events in the Tien Shan, Kyrgyzstan. Econ Geol 99:1771-1780

789 McClenaghan MB, Kjarsgaard BA (2007) Indicator mineral and surficial geochemical exploration methods for kimberlite in
790 glaciated terrain; Examples from Canada In: Goodfellow WD (ed) Mineral Deposits of Canada: A Synthesis of Major
791 Deposit-Types, District Metallogeny, the Evolution of Geological Provinces, and Exploration Methods. Geological
792 Association of Canada, Mineral Deposits Division,

793 McClenaghan MB, Cabri LJ (2011) Review of gold and platinum group element (PGE) indicator minerals methods for
794 surficial sediment sampling. Geochem: Explor, Environ, Anal 11:251-263

795 McDonough WF, Sun Ss (1995) The composition of the Earth. Chem Geol 120:223-253

796 Mortensen JK, Craw D, MacKenzie DJ, Gabites JE, Ullrich T (2010) Age and origin of orogenic gold mineralization in the
797 Otago schist belt, South Island, New Zealand; constraints from lead isotope and (super 40) Ar/ (super 39) Ar dating
798 studies. *Econ Geol* 105:777-793

799 Mueller AG (1991) The Savage Lode magnesian skarn in the Marvel Loch gold-silver mine, Southern Cross greenstone belt,
800 Western Australia; Part 1, Structural setting, petrography, and geochemistry. *Can J Earth Sci* 28:659-685

801 Mueller AG, De Laeter JR, Groves DI (1991a) Strontium isotope systematics of hydrothermal minerals from epigenetic
802 Archean gold deposits in the Yilgarn Block, Western Australia. *Econ Geol* 86:780-809

803 Mueller AG, Groves DI, Delor CP (1991b) The Savage Lode magnesian skarn in the Marvel Loch gold-silver mine, Southern
804 Cross greenstone belt, Western Australia; Part 2, Pressure-temperature estimates and constraints on fluid sources.
805 *Can J Earth Sci* 28:686-705

806 Mueller AG (1992) Petrogenesis of amphibole-biotite-calcite-plagioclase alteration and laminated gold-silver quartz veins in
807 four Archean shear zones of the Norseman District, Western Australia. *Canadian Journal of Earth Sciences = Revue*
808 *Canadienne des Sciences de la Terre* 29:388-417

809 Mueller AG (1997) The Nevoria gold skarn deposit in Archean iron-formation, Southern Cross greenstone belt, Western
810 Australia; I, Tectonic setting, petrography, and classification. *Econ Geol* 92:181-209

811 Mueller AG, Nemchin AA, Frei R (2004) The Nevoria gold skarn deposit, Southern Cross greenstone belt, Western Australia;
812 II, Pressure-temperature-time path and relationship to postorogenic granites. *Econ Geol* 99:453-478

813 Mueller AG (2015) Structure, alteration, and geochemistry of the Charlotte quartz vein stockwork, Mt Charlotte gold mine,
814 Kalgoorlie, Australia; time constraints, down-plunge zonation, and fluid source. *Miner Deposita* 50:221-244

815 Nassau K (1963) Calcium tungstate—IV: The theory of coupled substitution. *J Phys Chem Solids* 24:1511-1517

816 Nassau K, Loiacono GM (1963) Calcium tungstate—III: Trivalent rare earth substitution. *J Phys Chem Solids* 24:1503-1510

817 Peltonen P, Huhta P, Korsman K (1992) Occurrence and mineral chemistry of chrome spinel in till - implications for
818 prospecting magmatic Ni-Cu sulfide ores in Svecofennian terrain. Geological Survey of Finland,

819 Peng J, Zhang D, Hu R, Wu M, Lin Y (2010) Sm/Nd and Sr isotope geochemistry of hydrothermal scheelite from the Zhazixi
820 W-Sb deposit, western Hunan. *Acta Geol Sinica* 82:1514-1521

821 Poulin R, S. (2016) A study of the crystal chemistry, cathodoluminescence, geochemistry and oxygen isotopes in scheelite:
822 Application towards discriminating among differing ore-deposit systems *Geology*. Laurentian University, Sudbury,
823 Ontario, Canada

824 Poulin R, S., McDonald AM, Kontak DJ, McClenaghan MB (2016) On the Relationship Between Cathodoluminescence and
825 the Chemical Composition of Scheelite From Geologically Diverse Ore-Deposit Environments. *Can Mineral*
826 54:1147-1173

827 Poulin RS, Kontak DJ, McDonald A, McClenaghan MB (2018) Assessing scheelite as an ore-deposit discriminator using its
828 trace-element and REE chemistry. *The Canadian Mineralogist* 56:265-302

829 Raimbault L, Baumer A, Dubru M, Benkerrou C, Croze V, Zahm A (1993) REE fractionation between scheelite and apatite
830 in hydrothermal conditions. *Am Mineral* 78:1275-1285

831 Ren YS, Zhao HL, Lei E, Wang H, Ju N, Wu CZ (2010) Trace element and rare earth element geochemistry of the scheelite
832 and ore genesis of the Yangjingou large scheelite deposit in Yanbian area, northeastern China. *China Acta Petrol Sin*
833 26:3720–3726

834 Ridley JR, Diamond LW (2000) Fluid Chemistry of Orogenic Lode Gold Deposits and Implications for Genetic Models In:
835 Hagemann SG, Brown PE (eds) *Gold in 2000 - Reviews in Economic Geology* 13. Society of Economic Geologists,

836 Roberts S, Palmer MR, Waller L (2006) Sm-Nd and REE characteristics of tourmaline and scheelite from the Bjorkdal gold
837 deposit, northern Sweden: Evidence of an intrusion-related gold deposit? *Econ Geol* 101:1415-1425

838 Scanlan EJ, Scott JM, Wilson VJ, Stirling CH, Reid MR, Le Roux PJ (2018) In situ (super 87) Sr/ (super 86) Sr of scheelite
839 and calcite reveals proximal and distal fluid-rock interaction during orogenic W-Au mineralization, Otago Schist,
840 New Zealand. *Econ Geol* 113:1571-1586

841 Schwebel PJ, King P, Eisenlohr BN (1995) Edwards Find gold deposit Southern Cross greenstone belt - Geology and gold
842 mines. *Southern Cross, Western Australia*, pp 75-80

843 Shi W, Fleet ME, Sheih SR (2012) High-pressure phase transitions in Ca-Mn carbonates (Ca,Mn)CO₃ studied by Raman
844 spectroscopy. *Am Mineral* 97:999-1001

845 Shoji T, Sasaki N (1978) Fluorescent color and X-ray powder data of synthesized scheelite-powellite series as guides to
846 determine its composition. *Kozan Chishitsu = Mining Geology* 28, (6):397-404

847 Somarin AK (2004) Garnet composition as an indicator of Cu mineralization: evidence from skarn deposits of NW Iran. *J*
848 *Geochem Explor* 81:47-57

849 Song G, Qin K, Li G, Evans NJ, Chen L (2014) Scheelite elemental and isotopic signatures; implications for the genesis of
850 skarn-type W-Mo deposits in the Chizhou area, Anhui Province, eastern China. *Am Mineral* 99:303-317

851 Sun K, Chen B (2017) Trace elements and Sr-Nd isotopes of scheelite; implications for the W-Cu-Mo polymetallic
852 mineralization of the Shimensi Deposit, south China. *Am Mineral* 102:1114-1128

853 Sverjensky DM (1984) Europium redox equilibrium in aqueous solutions. *Earth Planet Sci Lett* 67:70-78

854 Sylvester PJ, Ghaderi M (1997) Trace element analysis of scheelite by excimer laser ablation-inductively coupled plasma-
855 mass spectrometry (ELA-ICP-MS) using a synthetic silicate glass standard. *Chem Geol* 141:49-65

856 Toverud Ö (1984) Dispersal of tungsten in glacial drift and humus in Bergslagen, southern central Sweden. *J Geochem Explor*
857 21:261-272

858 Tyson RM, Hemphill WR, Theisen AF (1988) Effect of the W:Mo ratio on the shift of excitation and emission spectra in the
859 scheelite-powellite series. *Am Mineral* 73:1145-1154

860 Uspensky E, Brugger J, Graeser S (1998) REE geochemistry systematics of scheelite from the Alps using luminescence
861 spectroscopy: from global regularities to local control. *Schweizerische Mineralogische Und Petrographische*
862 *Mitteilungen* 78:31-54

863 Van Horn FR (1930) Replacement of wolframite by scheelite with observations on the fluorescence of certain tungsten
864 minerals. *Am Mineral* 15:461-469

865 Voicu G, Bardoux M, Stevenson R, Jebrak M (2000) Nd and Sr isotope study of hydrothermal scheelite and host rocks at
866 Omai, Guiana Shield: implications for ore fluid source and flow path during the formation of orogenic gold deposits.
867 *Miner Deposita*

868 Xiong DX, Sun XM, Shi GY, Wang SW, Gao JF, Xue T (2006) Trace elements, rare earth elements (REE) and Nd-Sr isotopic
869 compositions in scheelites and their implications for the mineralization in Daping gold mine in Yunnan province,
870 China. *China Acta Petrol Sin* 22:733-741

871 Zhigang Z, Chaoyang L, Yuping L, Guangzhi T (1998) REE geochemistry of scheelite of two genetic types from Nanyangtian,
872 southeastern Yunnan, China. *Geology-Geochemistry* 26:34-38

873

Figure 1

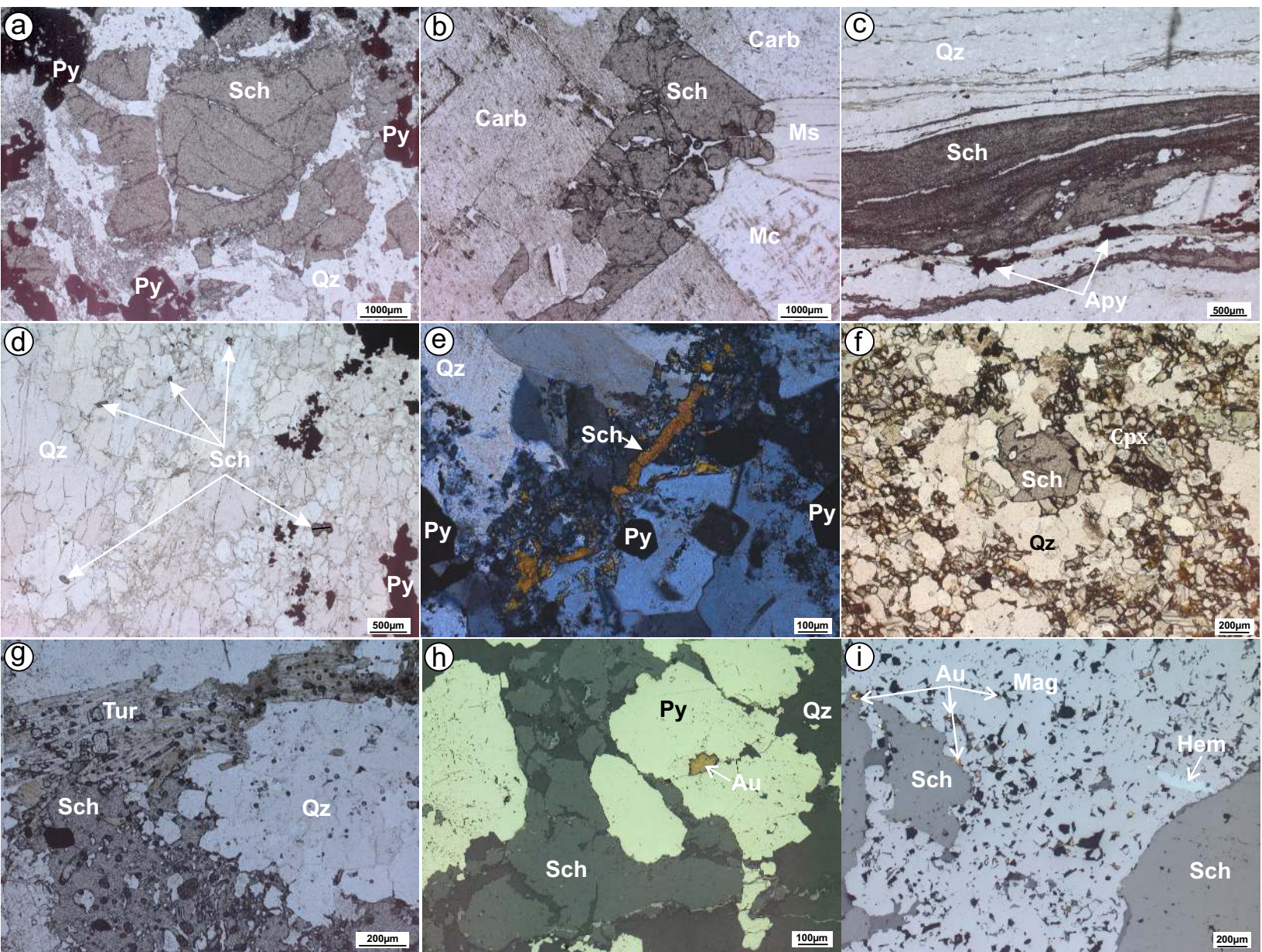


Figure 2

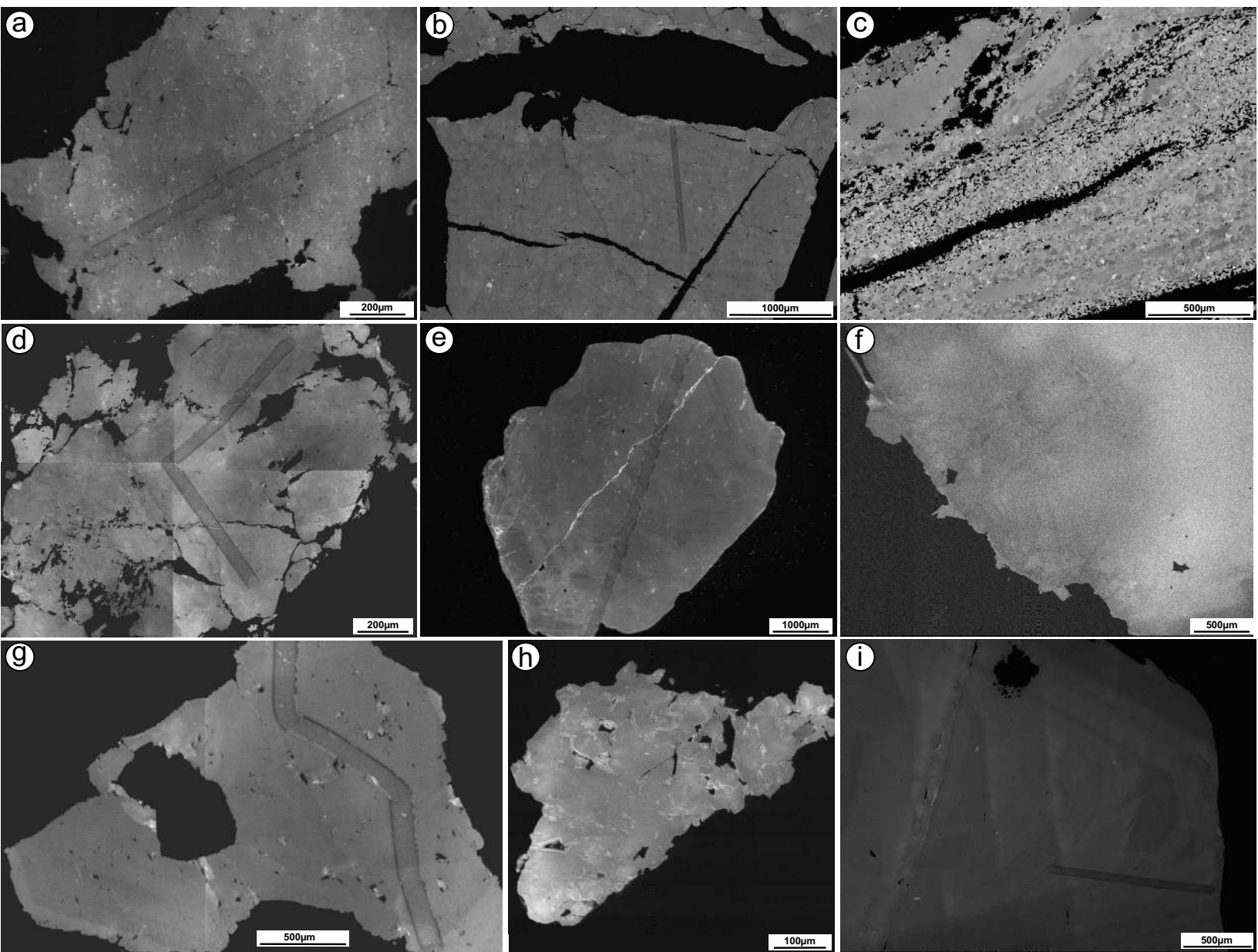


Figure 3

Figure 3

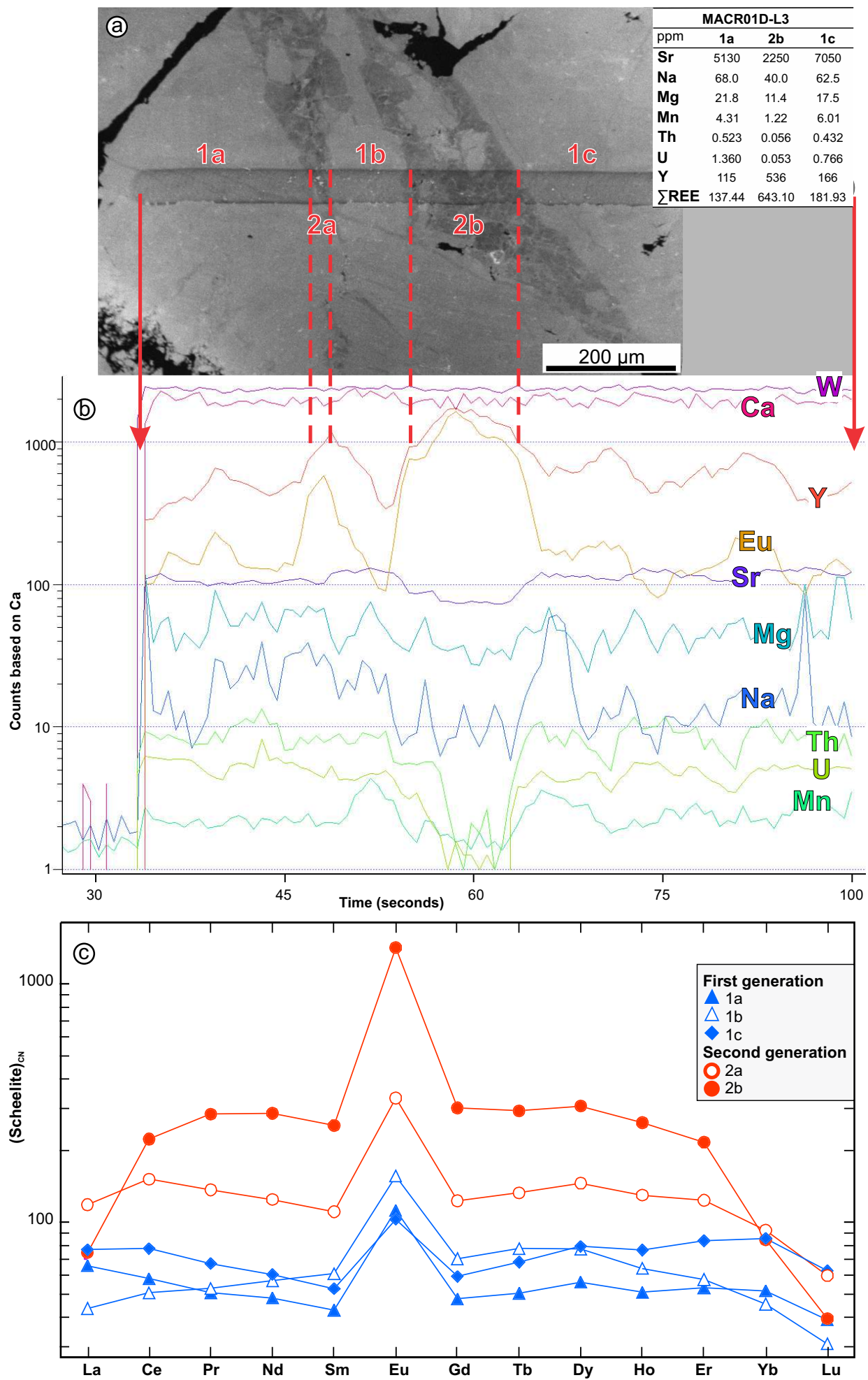


Figure 4

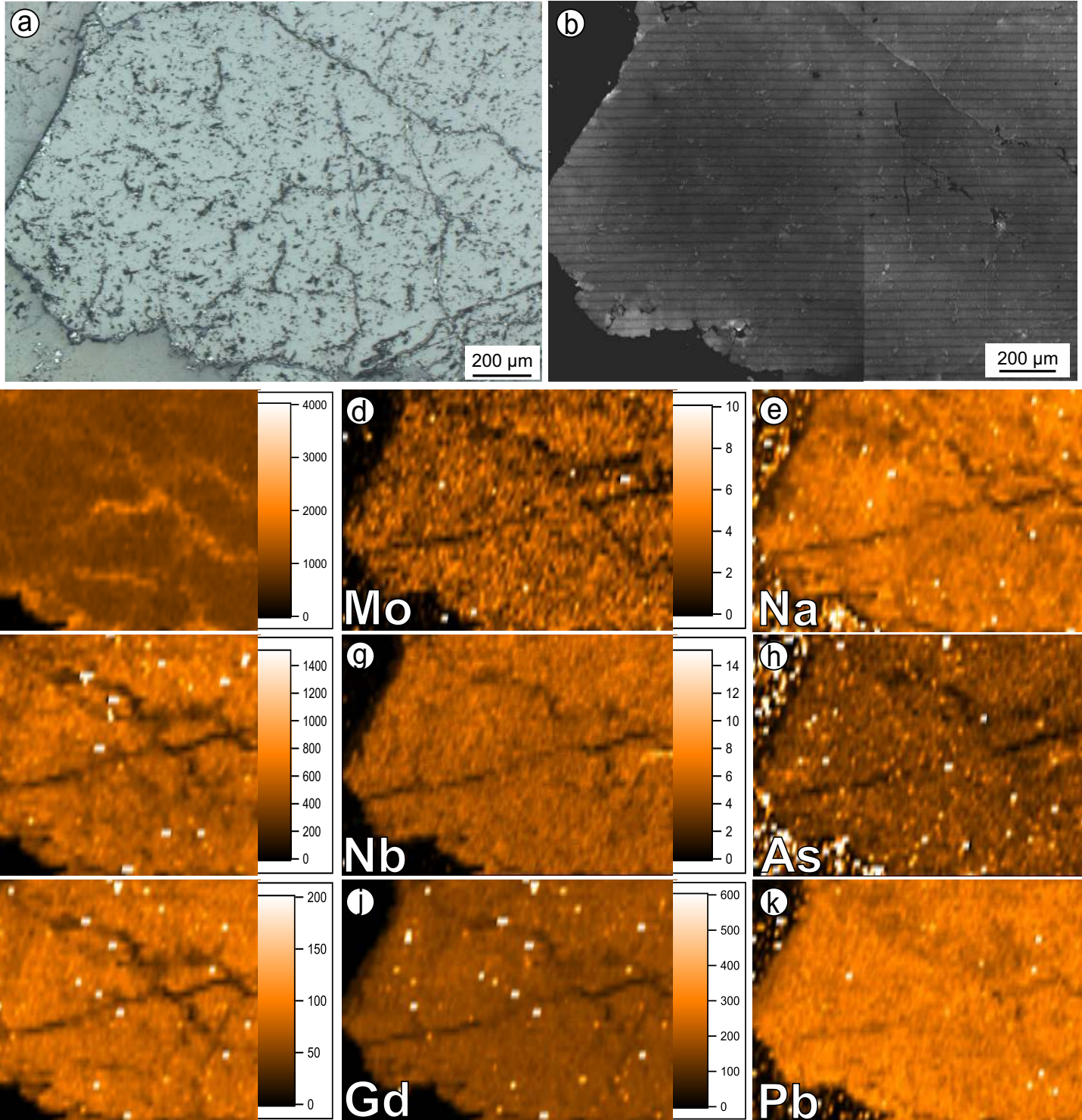


Figure 5

Figure 5

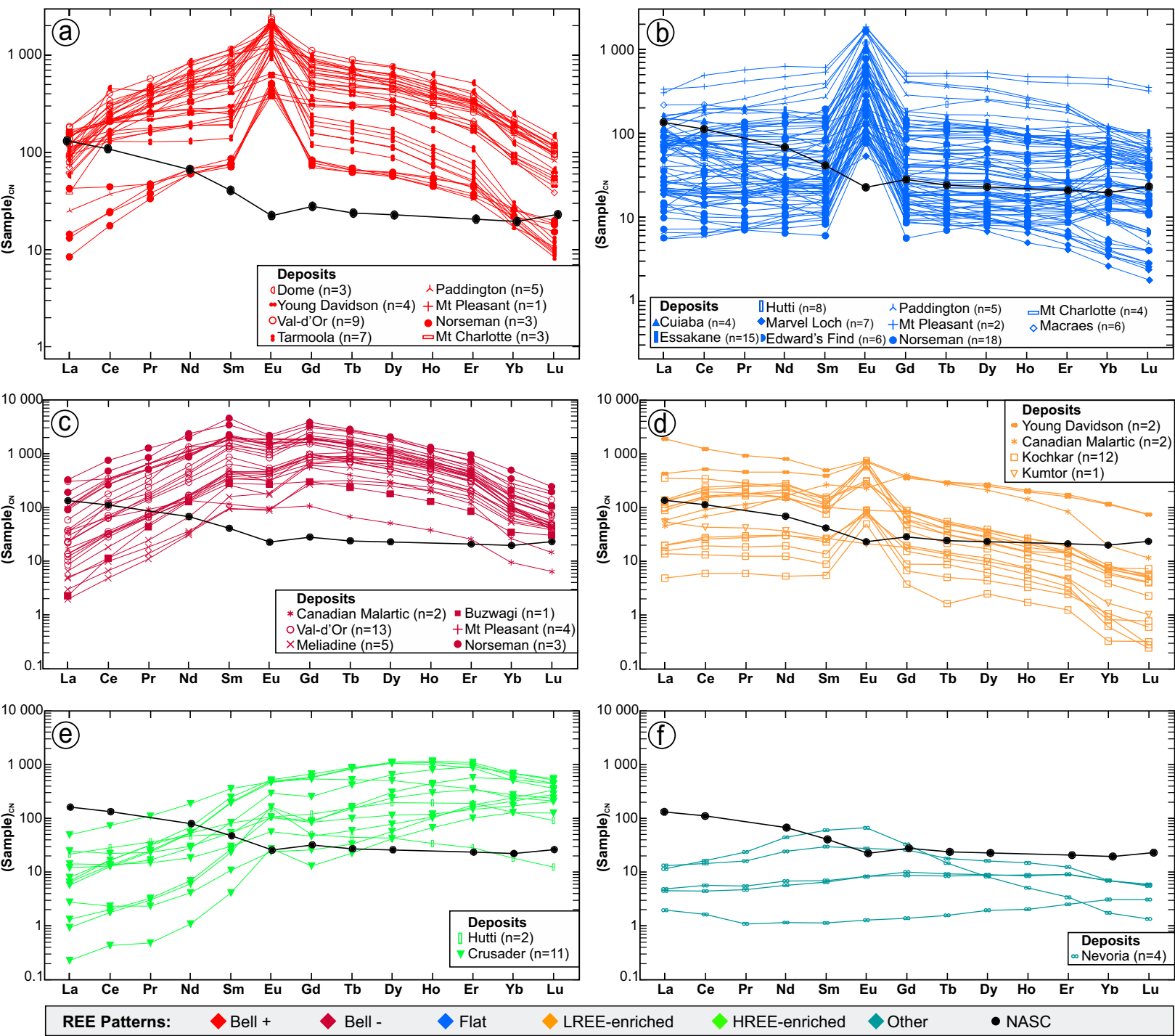


Figure 6

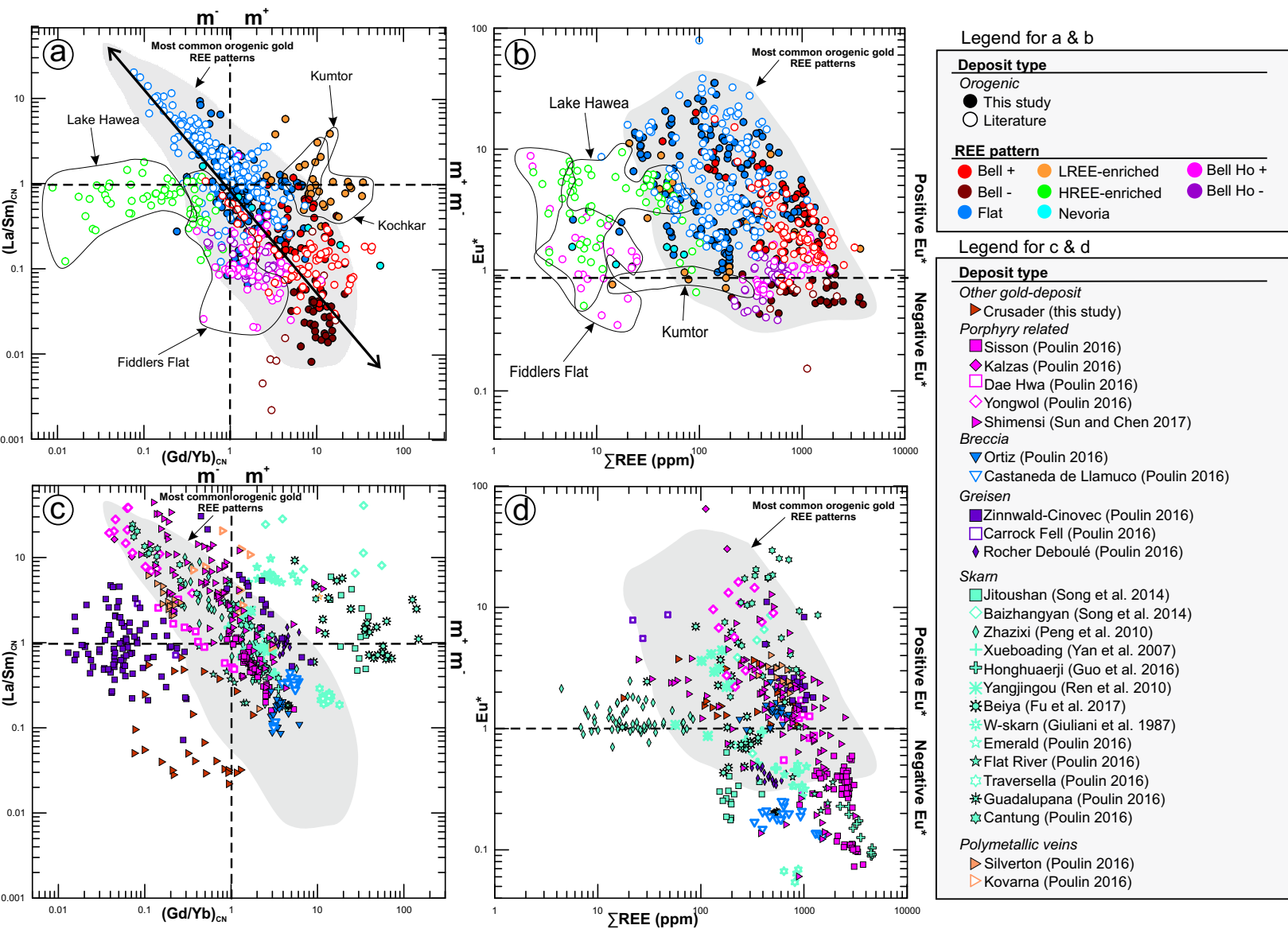
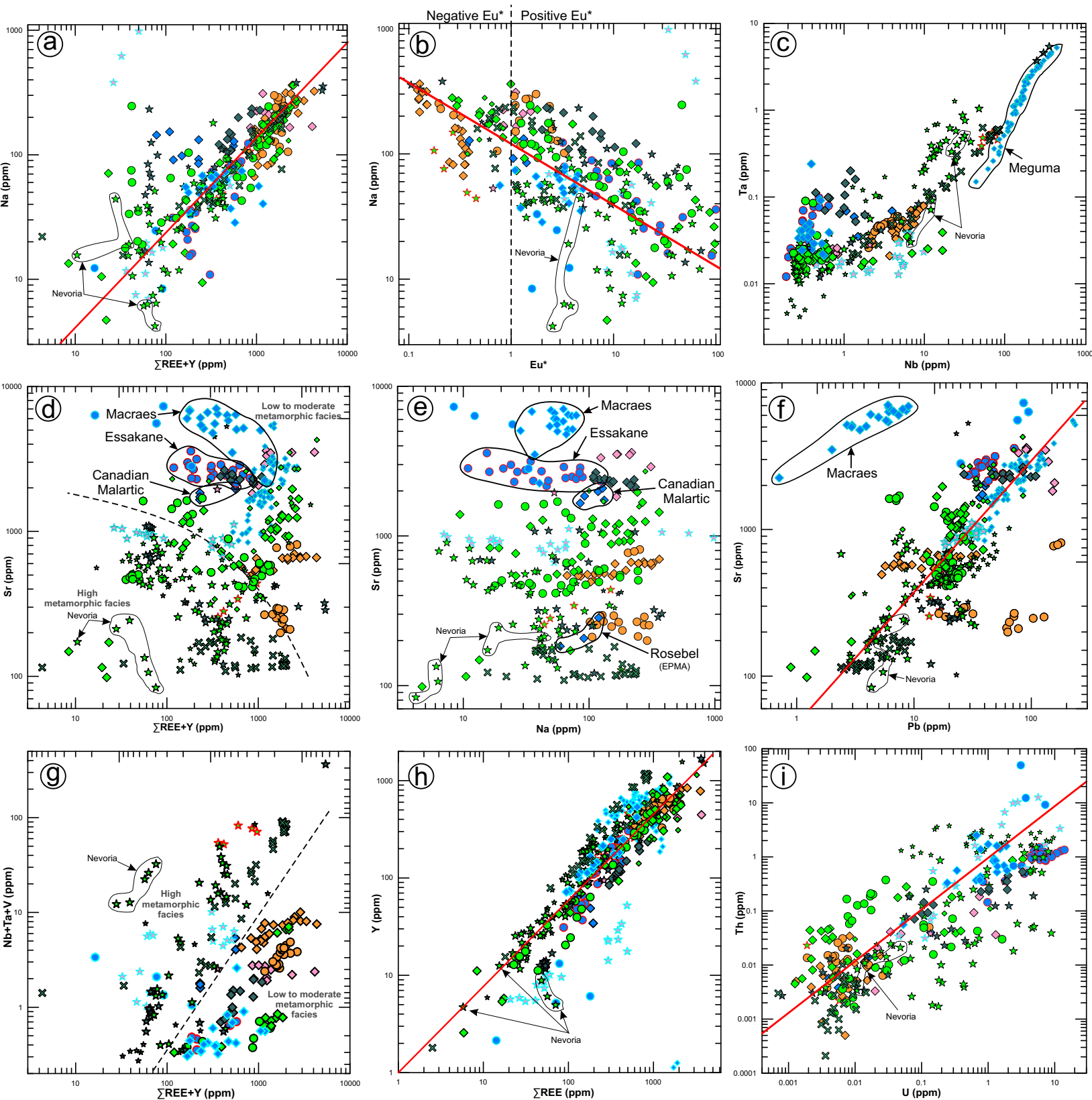


Figure 7

Figure 7

**Orogenic gold deposits****Origin**

- This study
- Literature

Metamorphic facies

- Low
- ◇ Moderate
- ☆ High

Mineralization age

- Archean
- Proterozoic
- Phanerozoic

Host rock composition

- Sedimentary
- Felsic
- Mafic
- Intermediate
- Ultramafic

Other gold deposit

- × Crusader

Figure 8

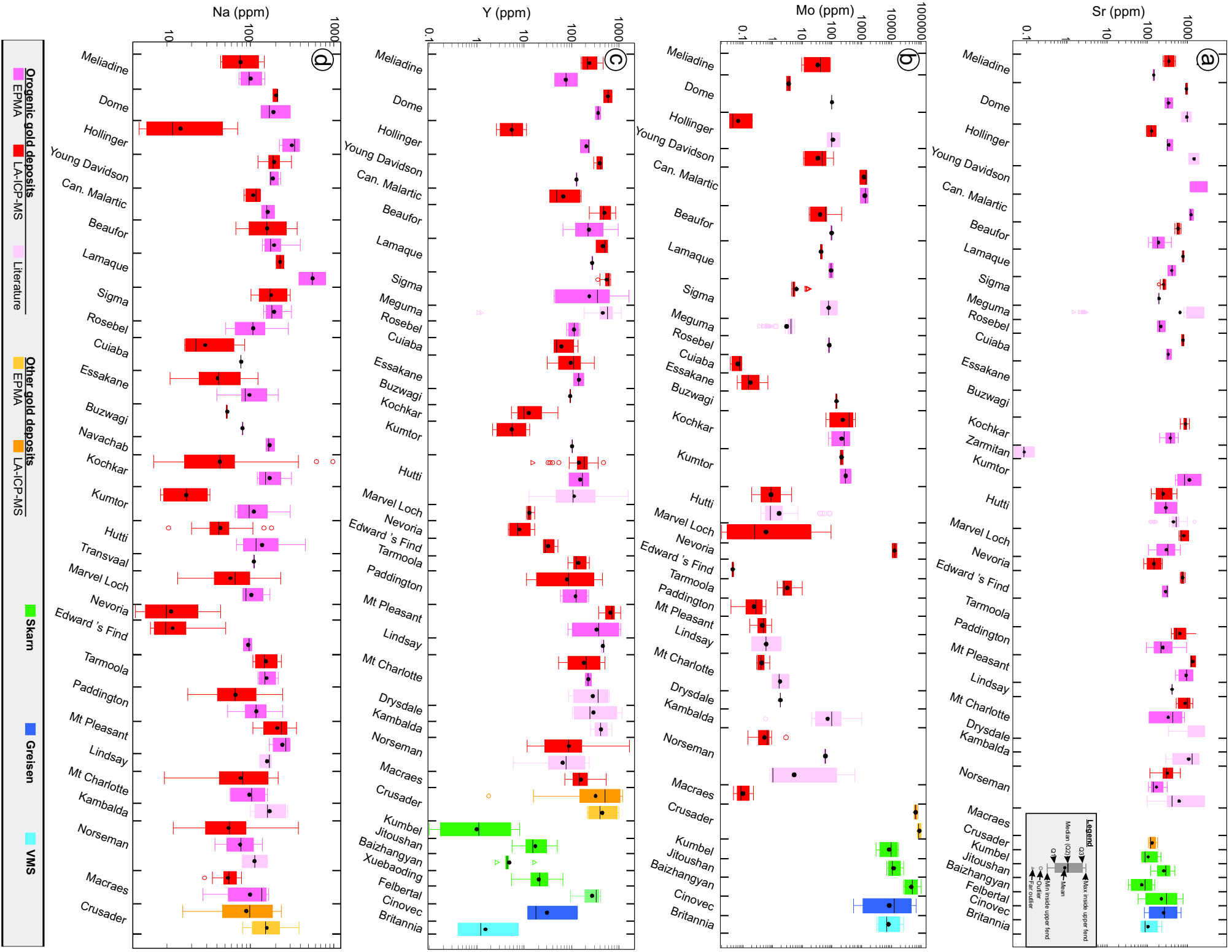


Figure 8

Figure 9

Figure 9

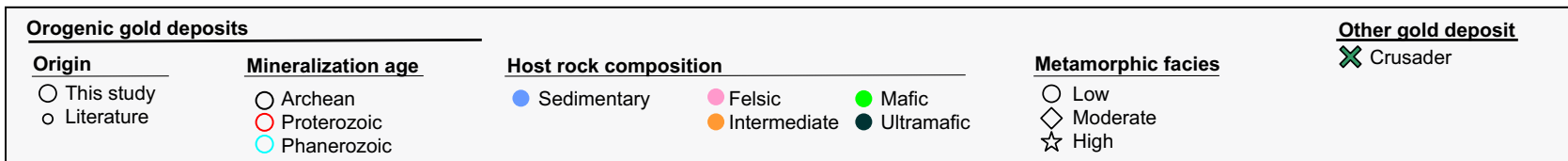
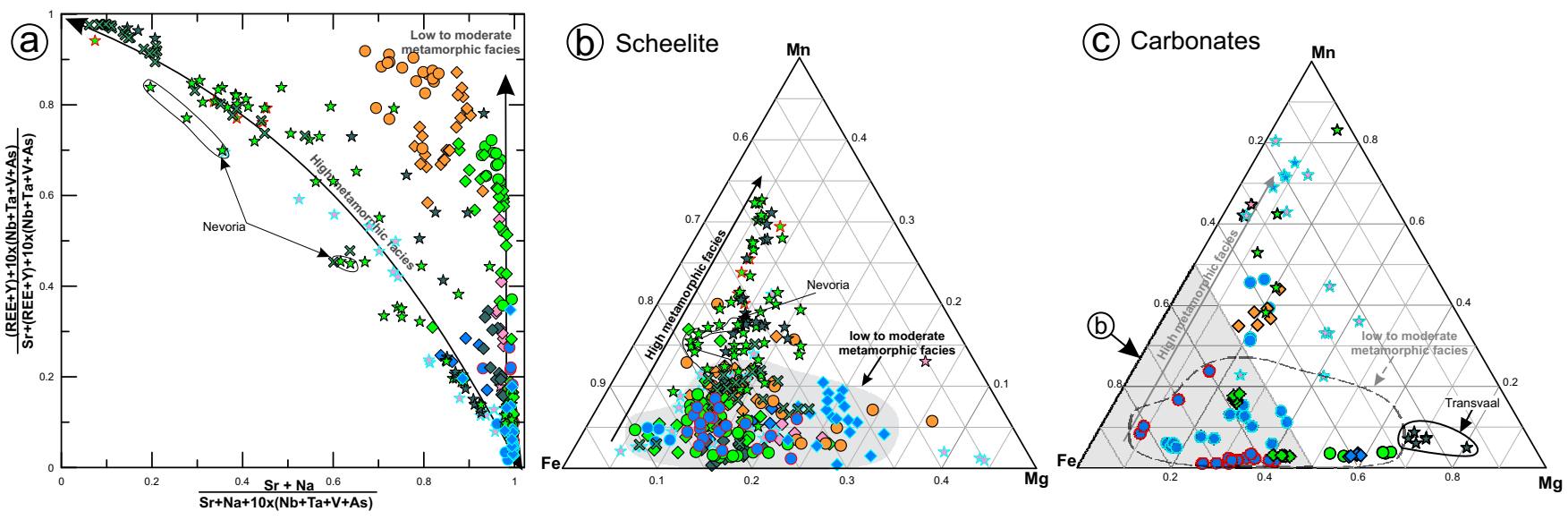


Figure 10

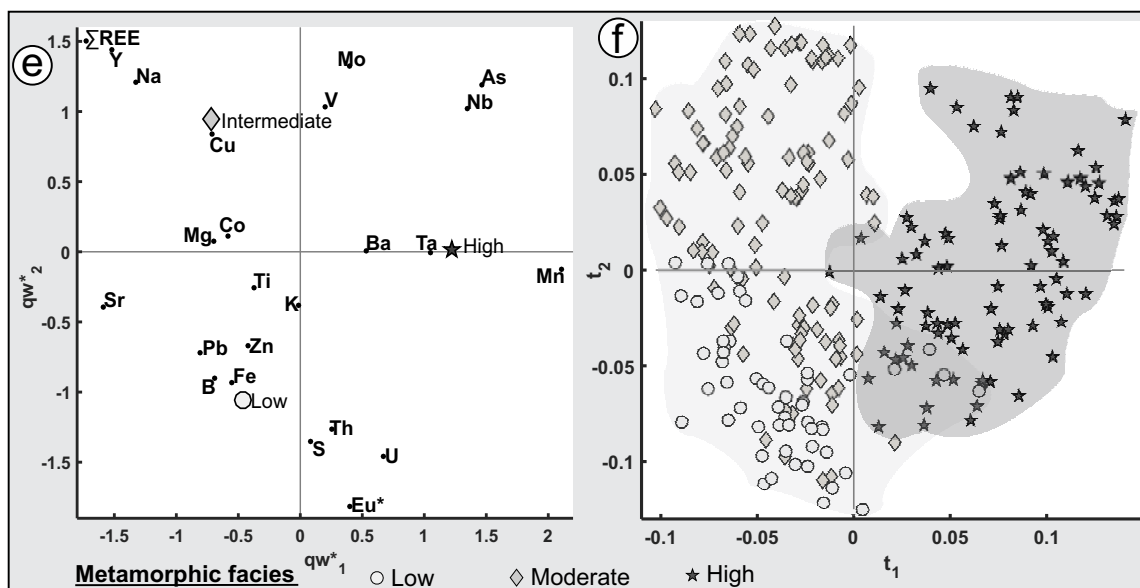
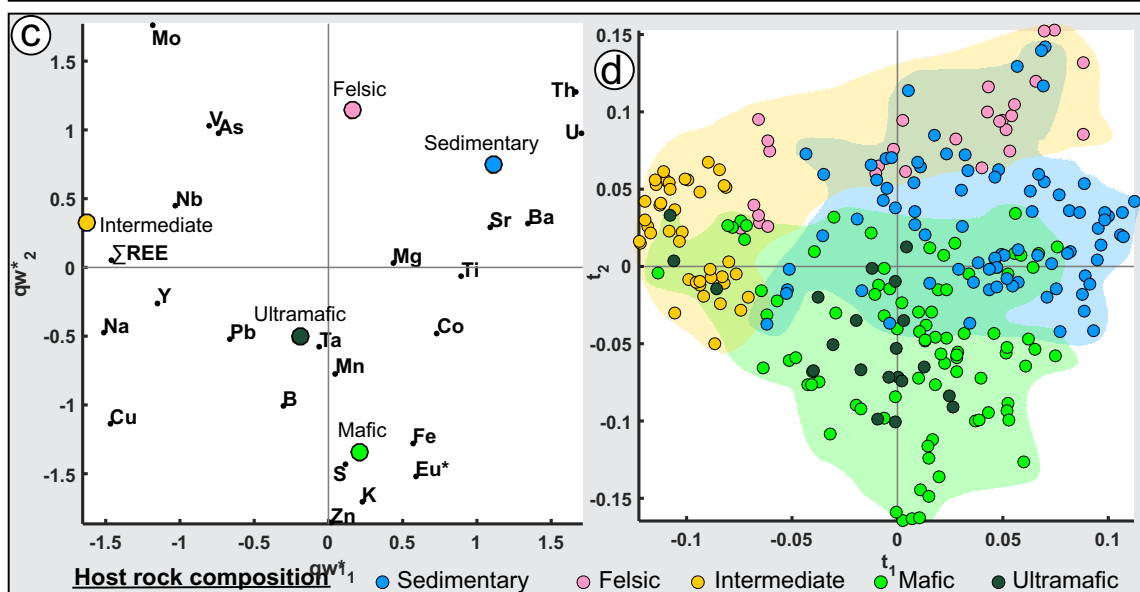
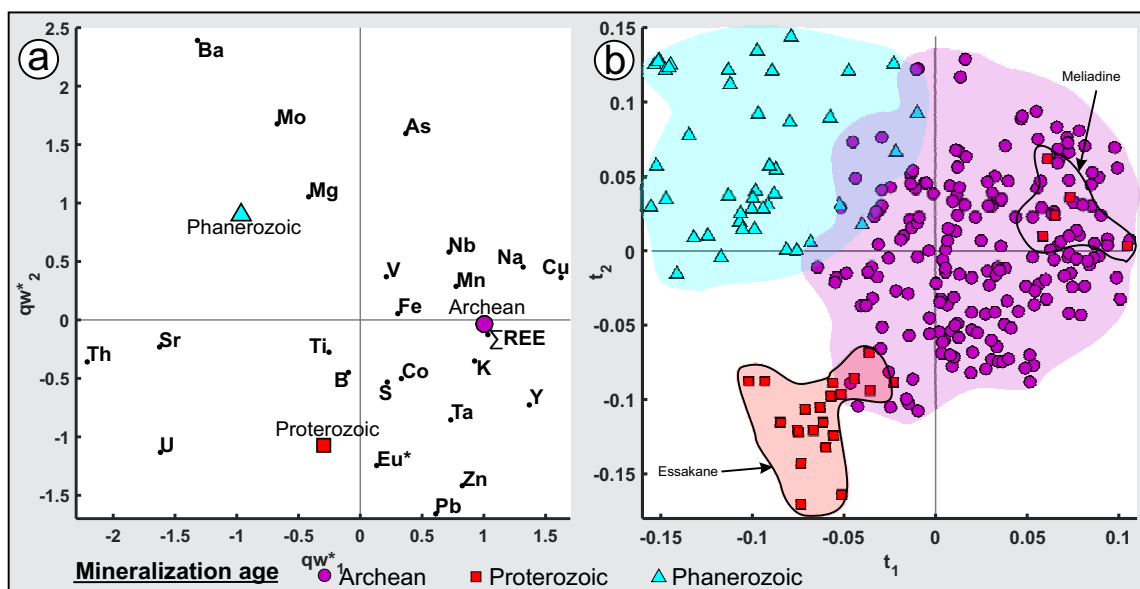
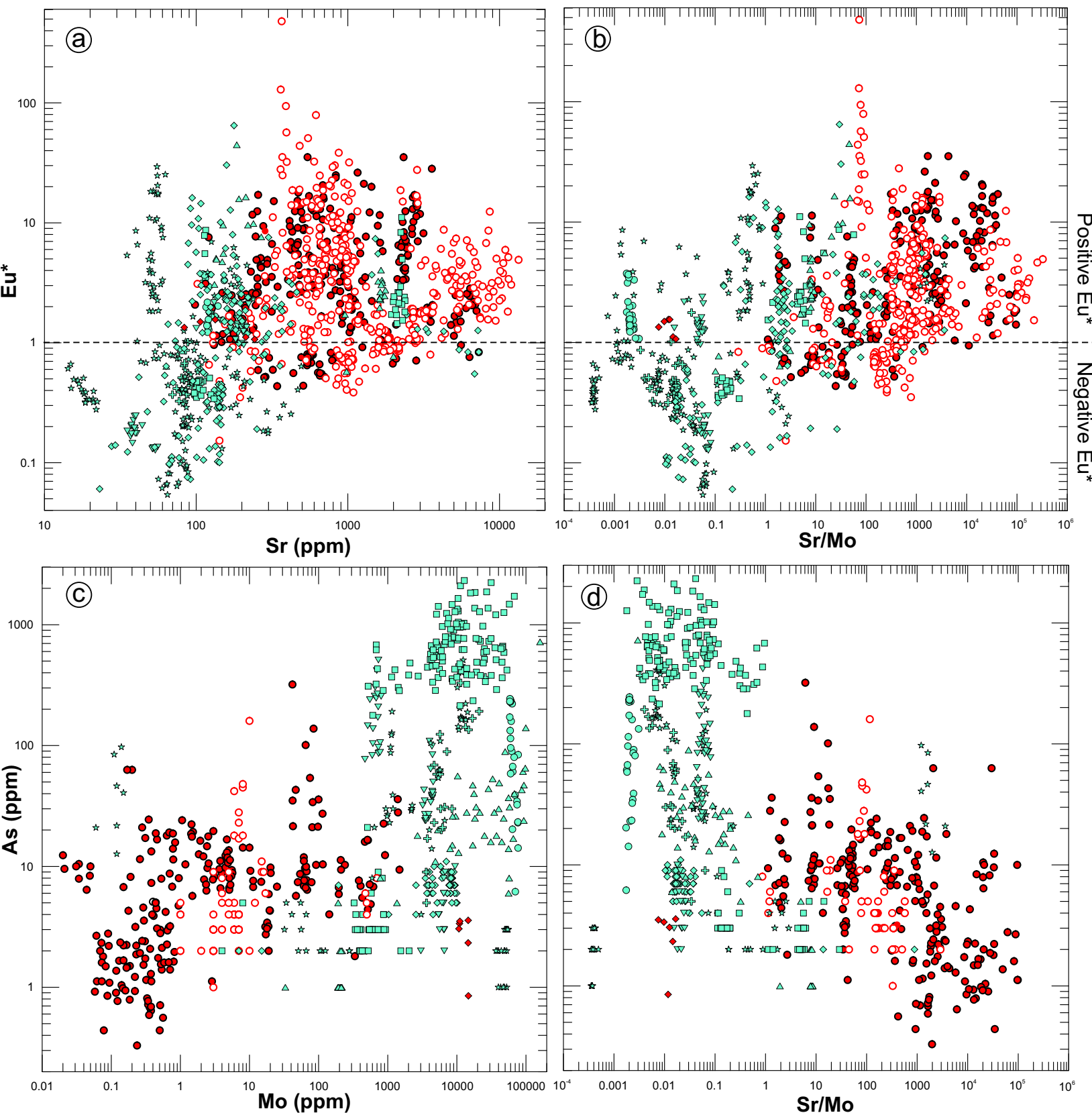


Figure 11

Figure 11

**Orogenic**

- This study
- Literature
- ◆ Nevoria (This study)

Other deposit types

- Other gold deposit (This study)
- ◇ Porphyry-related (Literature)
- Greisen (Poulin 2016)

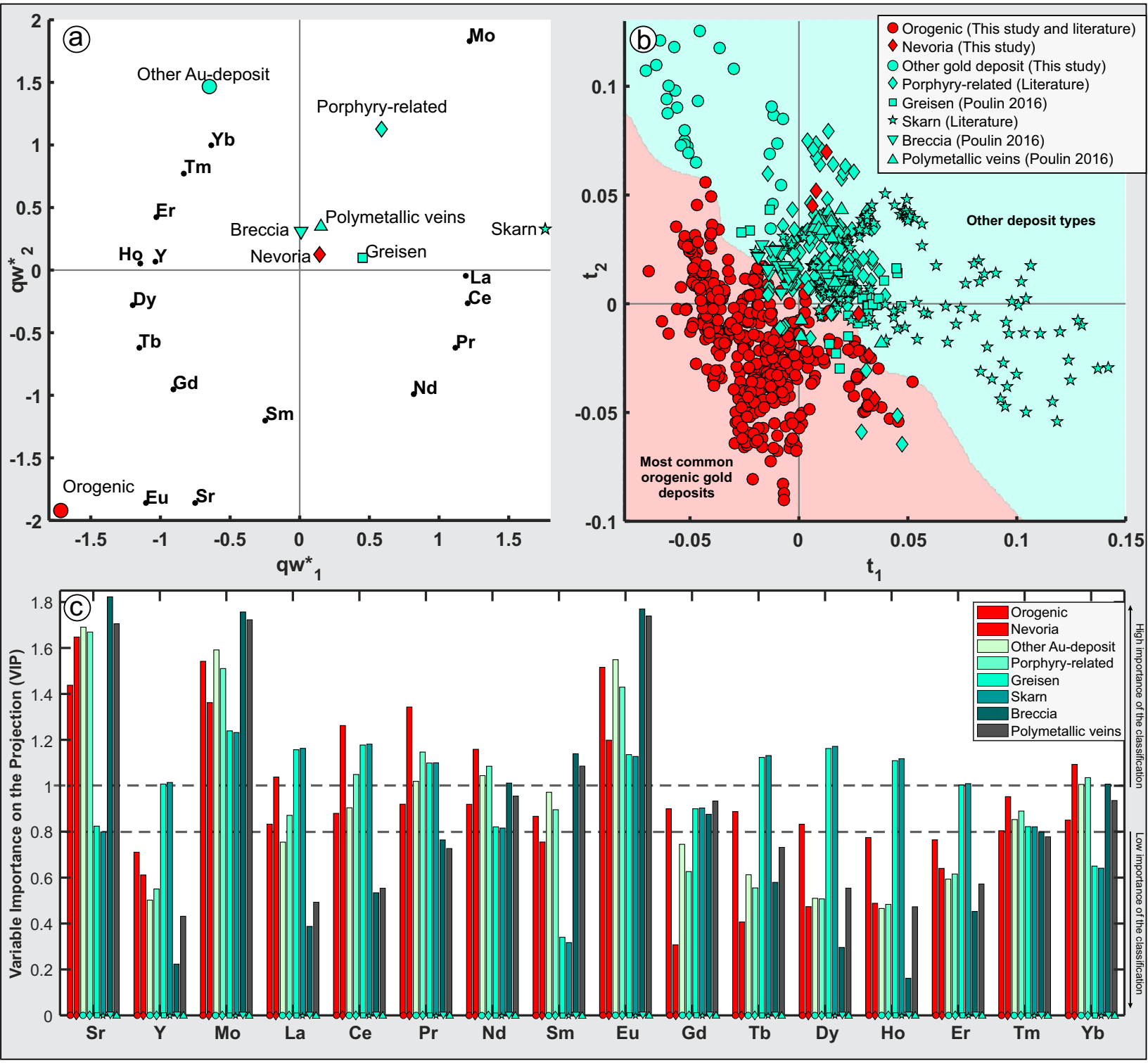
- ★ Skarn (Literature)

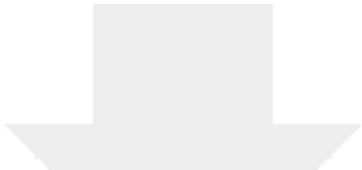
- ▼ Breccia (Poulin 2016)

- ▲ Polymetallic veins (Poulin 2016)


- ⊕ VMS (Poulin 2016)

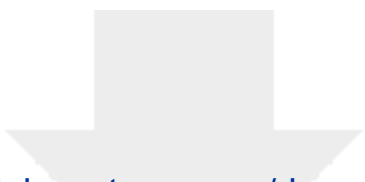
Figure 12



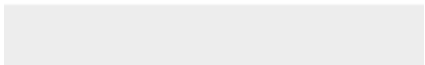



Click here to access/download
Supplementary Material
ESM01.pdf





Click here to access/download
Supplementary Material
ESM02.xlsx





Click here to access/download
Supplementary Material
ESM03.pdf

